THE UNIVERSITY of EDINBURGH

Edinburgh Research Explorer

Precise Masses and Orbits for Nine Radial Velocity Exoplanets

Citation for published version:
Li, Y, Brandt, TD, Brandt, GM, Dupuy, TJ, Michalik, D, Jensen-Clem, R, Zeng, Y, Faherty, J & Mitra, EL 2021, 'Precise Masses and Orbits for Nine Radial Velocity Exoplanets', *Astronomical Journal*, vol. 162, no. 6, 266, pp. 1-20. https://doi.org/10.3847/1538-3881/ac27ab

Digital Object Identifier (DOI):
10.3847/1538-3881/ac27ab

Link:
Link to publication record in Edinburgh Research Explorer

Document Version:
Peer reviewed version

Published In:
Astronomical Journal

General rights
Copyright for the publications made accessible via the Edinburgh Research Explorer is retained by the author(s) and / or other copyright owners and it is a condition of accessing these publications that users recognise and abide by the legal requirements associated with these rights.

Take down policy
The University of Edinburgh has made every reasonable effort to ensure that Edinburgh Research Explorer content complies with UK legislation. If you believe that the public display of this file breaches copyright please contact openaccess@ed.ac.uk providing details, and we will remove access to the work immediately and investigate your claim.

OPEN ACCESS

Download date: 19. Apr. 2024

Draft version October 5, 2021
Typeset using LaTeX twocolumn style in AASTeX63

arXiv:2109.10422v2 [astro-ph.EP] 4 Oct 2021

Precise Masses and Orbits for Nine Radial Velocity Exoplanets

Yiting Li,[1] Timothy D. Brandt,[1] G. Mirek Brandt,[1,*] Trent J. Dupuy,[2] Daniel Michalik,[3] Rebecca Jensen-Clem,[4] Yunlin Zeng,[5] Jacqueline Faherty,[6] and Elena L. Mitra[7]

[1] *Department of Physics, University of California, Santa Barbara, Santa Barbara, CA 93106, USA*
[2] *Institute for Astronomy, University of Edinburgh, Royal Observatory, Blackford Hill, Edinburgh, EH9 3HJ, UK*
[3] *European Space Agency (ESA), European Space Research and Technology Centre (ESTEC), Keplerlaan 1, 2201 AZ Noordwijk, The Netherlands*
[4] *Astronomy & Astrophysics Department, University of California, Santa Cruz, CA 95064, USA*
[5] *School of Physics, Georgia Institute of Technology, 837 State Street, Atlanta, Georgia, USA*
[6] *American Museum of Natural History, New York, NY*
[7] *CUNY Hunter College, New York, NY 10065, USA*

ABSTRACT

Radial velocity (RV) surveys have discovered hundreds of exoplanetary systems but suffer from a fundamental degeneracy between planet mass M_p and orbital inclination i. In this paper we break this degeneracy by combining RVs with complementary absolute astrometry taken from the *Gaia* EDR3 version of the cross-calibrated *Hipparcos-Gaia* Catalog of Accelerations (HGCA). We use the Markov Chain Monte Carlo orbit code `orvara` to simultaneously fit literature RVs and absolute astrometry from the HGCA. We constrain the orbits, masses, and inclinations of nine single and massive RV companions orbiting nearby G and K stars. We confirm the planetary nature of six companions: HD 29021 b ($4.47^{+0.67}_{-0.65} M_{\rm Jup}$), HD 81040 b ($7.24^{+1.0}_{-0.37} M_{\rm Jup}$), HD 87883 b ($6.31^{+0.31}_{-0.32} M_{\rm Jup}$), HD 98649 b ($9.7^{+2.3}_{-1.9} M_{\rm Jup}$), HD 106252 b ($10.00^{+0.78}_{-0.73} M_{\rm Jup}$), and HD 171238 b ($8.8^{+3.6}_{-1.3} M_{\rm Jup}$). We place one companion, HD 196067 b ($12.5^{+2.5}_{-1.8} M_{\rm Jup}$) on the planet-brown dwarf boundary, and two companions in the low mass brown dwarf regime: HD 106515 Ab ($18.9^{+1.5}_{-1.4} M_{\rm Jup}$), and HD 221420 b ($20.6^{+2.0}_{-1.6} M_{\rm Jup}$). The brown dwarf HD 221420 b, with a semi-major axis of $9.99^{+0.74}_{-0.70}$ AU, a period of $27.7^{+3.0}_{-2.5}$ years, and an eccentricity of $0.162^{+0.035}_{-0.030}$ represents a promising target for high-contrast imaging. The RV orbits of HD 87883 b, HD 98649 b, HD 171238 b, and HD 196067 b are not fully constrained yet because of insufficient RV data. We find two possible inclinations for each of these orbits due to difficulty in separating prograde from retrograde orbits, but we expect this will change decisively with future Gaia data releases.

Keywords: —

1. INTRODUCTION

The radial velocity (RV) technique is one of the earliest and most commonly used indirect methods in the detection of exoplanets in both nearby and distant solar systems (Hatzes 2016; Wei 2018; Wright 2018). 51 Pegasi b, the first exoplanet around a Sun-like star, was discovered via RV in 1995 (Mayor & Queloz 1995). Since then, RV instruments have overcome many design and performance challenges to reach extreme m/s precisions, at once revealing the richness and diversity of the population of exoplanets (e.g. Udry et al. 2007; Akeson et al. 2013; Rice 2014).

The RV method measures the Doppler shift in the spectrum of a star perturbed by one or multiple unseen orbiting companions (Walker 2012; Plavchan et al. 2015; Fischer et al. 2016; Wright 2018). The RV semi-amplitude due to a companion scales with the companion's mass, the sine of the orbital inclination ($\sin i$), and the inverse of the square root of the semi-major axis. This means that massive and close-in RV companions are usually more easily and precisely characterized owing to complete orbital coverage. Much like 51 Pegasi b, these are often short-period Jupiter analogs orbiting solar-type stars (Wright et al. 2003).

Thanks to the growing temporal baselines of RV surveys, detection sensitivity is now being extended beyond the ice line ($\gtrsim$ 3 AU) (Ford 2014; Wittenmyer et al.

* NSF Graduate Research Fellow

2016). In this wider orbital regime, long-period giant planets are frequently being revealed (Perrier et al. 2003; Marmier et al. 2013; Rickman et al. 2019). Small planets or Uranus/Neptune-like ice giants on such wide orbits however are very challenging to detect due to long orbital periods (80-165 years), low transit probability, and the high contrast barrier. Still longer-period companions can induce measurable RV trends or accelerations (Eisner & Kulkarni 2001; Cumming 2004; Knutson et al. 2014). .

Not all stars are accessible to RV searches for planets. RV surveys often target old and inactive main sequence FGK stars and M dwarfs because their lower RV jitter and abundance of narrow absorption lines allow very precise velocity measurements (e.g. Howard et al. 2012; Marchwinski et al. 2014; Gaidos et al. 2016; Hsu et al. 2019; Borgniet et al. 2019; He et al. 2020; Bauer et al. 2020; Jin 2021). In addition, there are several limitations to using the RV method alone to characterize long period companions. Firstly, orbital phase coverage drives estimations of orbital periods, so the RVs must cover a significant fraction of an orbit which requires long term time commitments from RV-surveys. Secondly, RVs only constrain $M_p \sin i$, providing a minimum mass that is estimated assuming an edge-on system with $\sin i = 1$. This $\sin i$ degeneracy permits only a statistical estimate of a planet's true mass and limits our ability to understand an individual exoplanetary system (e.g., Batalha et al. 2019; Gaudi 2021).

One way to break the degeneracy in RV-only orbital fits is to combine RVs with precision astrometry. Astrometry measures the sky-projected Keplerian motion of accelerating stars. Together, radial velocity accelerations and astrometric accelerations probe orthogonal components of the 3D acceleration of a star through space, enabling us to map out the complete stellar reflex motion of a star under the influence of any unseen companion(s) (Lindegren & Dravins 2003).

Efforts to measure the reflex motion of stars astrometrically date back to the Fine Guidance Sensor (FGS) on the Hubble Space Telescope (HST). FGS/HST has achieved sub-milliarcsecond single-star optical astrometry precision (Benedict et al. 2008). Pioneering works incorporated HST/FGS observations in ground-based astrometric and radial velocity fits to derive true masses for exoplanetary systems (e.g., Benedict et al. 2002; Benedict et al. 2006; McArthur et al. 2010). Beyond FGS/HST, the recent advent of Gaia astrometry and long-baseline interferometry open up the possibility of identifying and characterizing accelerating systems more systematically and on a larger scale. In particular, the combination of proper motion data from *Hipparcos* and *Gaia* provides a powerful and unique opportunity to realize this.

Gaia (Gaia Collaboration 2020; Lindegren et al. 2020) and its predecessor *Hipparcos* (ESA 1997; van Leeuwen 2007) were launched by the European Space Agency (ESA) to map the absolute positions of stars across the celestial sphere. The data from both satellites are processed as least-squares solutions to model sky paths; the catalogs list the best-fit astrometric parameters such as proper motions and parallaxes along with their uncertainties and covariances. (Lindegren & Dravins 2003), *Hipparcos* and *Gaia* took data ∼25 years apart, and the positional difference between *Hipparcos* and *Gaia* divided by this temporal baseline offers a new and more precise proper motion. Comparing this third proper motion with either the *Hipparcos* or *Gaia* measurement indicates acceleration in an inertial frame. A cross-calibration between the *Hipparcos* and *Gaia* catalogs must first correct error underestimation and frame rotation. To achieve this, Brandt (2018) and Brandt (2021) have placed the *Hipparcos* and *Gaia* DR2 and EDR3 catalogs, respectively, in a common reference frame presented in the cross-calibrated *Hipparcos*-*Gaia* catalog of accelerations (HGCA). HGCA astrometry has the potential to break the $\sin i$ degeneracy in RV-detected companions.

Previous works have explored the idea of using *Hipparcos* epoch astrometry in conjunction with RVs or relative astrometry to obtain precise dynamical masses (e.g., Han et al. 2001; Sozzetti & Desidera 2010; Reffert & Quirrenbach 2011; Sahlmann et al. 2011). More recently, with the release of *Gaia* astrometry, a number of works have achieved improved astrometric/RV mass approximations by combining different data types: RV+relative astrometry (e.g., Brown 2011; Boffin et al. 2016), RV+absolute astrometry (e.g., Feng et al. 2019; Kervella et al. 2019; Venner et al. 2021), relative astrometry+absolute astrometry (e.g., Chen&Li et al., in prep), or RV+relative astrometry+absolute astrometry (Snellen & Brown 2018; Brandt et al. 2019; Grandjean et al. 2019; Brandt et al. 2020; Nielsen et al. 2020; Brandt et al. 2021a; Kiefer et al. 2021; Brandt et al. 2021b, e.g.,).

In this paper, we derive orbital solutions for nine RV-detected exoplanet candidates by jointly analyzing RVs and complementary absolute astrometry data from the HGCA (Gaia EDR3 version): HD 29021, HD 81040, HD 87883, HD 98649, HD 106252, HD 106515 A, HD 171238, HD 196067, and HD 221420. We use the MCMC orbit-fitting package `orvara` (Brandt et al. 2021c) that is capable of fitting one or more Keplerian orbits to any combination of RVs, direct imaging

astrometry and absolute astrometry from the HGCA. Because the epoch astrometry from Gaia is not yet available, `orvara` uses the intermediate astrometry fitting package `htof` (Brandt et al. 2021b) to provide a workaround for this. `htof` fetches the intermediate astrometry from Hipparcos and Gaia, and reproduces positions and proper motions from synthetic Hipparcos or Gaia epoch astrometry using five or higher degree parameter fits. We focus our work on systems with known single RV companions. Two host stars in our sample, HD 106515 A and HD 196067, have known wide stellar companions that we solve as 3-body systems with `orvara`.

The paper is structured as follows. Section 2 presents our re-examination of the properties of the host stars, including a systematic re-analysis of the host stars' ages and masses based on an activity-age Bayesian model and PARSEC isochrones. Section 3 describes the literature radial velocity data we use to fit orbits. Section 4 discusses the stellar astrometry derived from the cross-calibrated *Hipparcos-Gaia* Catalog of Accelerations. In Section 6, we demonstrate the method we use to fit orbits to our sample of nine RV companions, followed by Section 7 where we show full orbital solutions from the orbital fits and discuss the implications of our work. We provide updated parameters, in particular, precise masses and inclinations for these planets in the same section. We summarize our results and findings in Section 8.

2. STELLAR CHARACTERISTICS

Table 1. Adopted stellar parameters for stars investigated in this work[a].

Star (HD #)	29021	81040	87883	98649	106252	106515A	106515B*	171238	196067	196068*	221420
HIP ID	21571	46076	49699	55409	59610	59743A	59743B	91085	102125	102128	116250
$\bar{\omega}$ (mas)	32.385	29.063	54.668	23.721	26.248	29.315	29.391	22.481	25.033	25.038	32.102
$\sigma[\bar{\omega}]$	0.024	0.041	0.030	0.022	0.027	0.030	0.029	0.032	0.021	0.017	0.033
V_T (mag)	7.842	7.791	7.660	8.066	7.479	8.063	8.298	8.737	6.510	7.070	5.884
$\sigma[V_T]$	0.011	0.012	0.012	0.011	0.011	0.014	0.015	0.020	0.010	0.010	0.009
B_T (mag)	8.612	8.527	8.800	8.793	8.158	8.994	9.284	9.589	7.193	7.790	6.643
$\sigma[B_T]$	0.016	0.017	0.018	0.017	0.017	0.021	0.022	0.029	0.015	0.015	0.014
K_s (mag)	6.082	6.159	5.314	6.419	5.929	6.151	6.267	6.831	5.080	5.713	4.306
$\sigma[K_s]$	0.020	0.021	0.020	0.020	0.026	0.026	0.017	0.017	0.016	0.018	0.036
J (mag)	6.518	6.505	5.839	6.811	6.302	6.585	6.746	7.244	5.417	6.061	4.997
$\sigma[J]$	0.029	0.019	0.020	0.019	0.024	0.024	0.030	0.019	0.021	0.027	0.252
R_X	< -5.14	-5.27	< -5.25	< -4.87	< -5.20	< -4.84	< -4.77	< -4.83	< -5.08	< -4.87	< -5.55
$R'_{\rm HK}$	...	-4.71	-4.98	-4.96	-4.85	-5.10	-5.15	-4.96	-5.06	-5.02	-5.05
$P_{\rm rot}$ (days)	...	15.98	...	26.441	...	...	...	...	...	...	...
[Fe/H](dex)[b]	-0.30 ± 0.10	-0.04 ± 0.05	0.11 ± 0.10	-0.06 ± 0.04	-0.06 ± 0.04	0.03 ± 0.10	0.03 ± 0.10	0.20 ± 0.10	0.23 ± 0.07	0.24 ± 0.10	0.34 ± 0.07
$M_{*,\rm model}(M_\odot)$[c]	0.86 ± 0.02	0.99 ± 0.02	0.80 ± 0.02	0.97 ± 0.02	1.05 ± 0.02	0.89 ± 0.03	0.86 ± 0.03	0.92 ± 0.03	1.26 ± 0.07	1.12 ± 0.06	1.28 ± 0.08
$L_*(L_\odot)$[d]	0.659 ± 0.017	0.838 ± 0.018	0.338 ± 0.008	0.968 ± 0.019	1.328 ± 0.030	0.686 ± 0.018	0.567 ± 0.017	0.627 ± 0.018	3.435 ± 0.068	2.007 ± 0.045	3.850 ± 0.072
Spectral Type	G5	G2/G3	K0	G3/G5 V	G0	G5 V	G8 V	G8 V	G5 III	G5 V	G2 V
Age (Gyr)[e]	$5.5^{+1.2}_{-1.0}$	$1.79^{+0.30}_{-0.26}$	$7.6^{+2.8}_{-1.8}$	$4.44^{+0.68}_{-0.58}$	$3.00^{+0.80}_{-0.60}$	$8.2^{+2.7}_{-2.1}$	$8.4^{+2.6}_{-2.1}$	$7.0^{+6.0}_{-1.6}$	$5.8^{+4.3}_{-2.2}$	$6.2^{+4.1}_{-2.2}$	$6.6^{+3.7}_{-2.0}$

* Secondary stellar companion

[a] **References** – $\bar{\omega}$ from Gaia eDR3 (Gaia Collaboration et al. 2020); V_T and B_T from Tycho-2 (Høg et al. 2000), K_s from 2MASS (Cutri et al. 2003); R_X from ROSAT (Voges et al. 1999); Rotation period for HD 81040 from Reinhold & Hekker (2020), alternatively 15.2579 days from Oelkers et al. (2018); $R'_{\rm HK}$ from (Pace 2013); Rotation period for HD 98649 from Oelkers et al. (2018); Spectral types from Wright et al. (2003) and Skiff (2014).

[b] We estimate [Fe/H] from the median of all entries in (Soubiran et al. 2016) with a default uncertainty of 0.1 dex. The references for each star are: Kim et al. (2016) for HD 29021; Sousa et al. (2006); Gonzalez et al. (2010); Kang et al. (2011); Luck (2017); Rich et al. (2017); Sousa et al. (2018) for HD 81040; Valenti & Fischer (2005); Kotoneva et al. (2006); Mishenina et al. (2008); Maldonado et al. (2012); Brewer et al. (2016); Luck (2017) for HD 87883; Datson et al. (2012); Santos et al. (2013); Porto de Mello et al. (2014); Ramírez et al. (2014); Rich et al. (2017) for HD 98649; Sadakane et al. (2002); Heiter & Luck (2003); Laws et al. (2003); Santos et al. (2003, 2004, 2005); Huang et al. (2005); Valenti & Fischer (2005); Luck & Heiter (2006); Takeda et al. (2007); Fuhrmann (2008); Gonzalez et al. (2010); Kang et al. (2011); Datson et al. (2015); Spina et al. (2016); Luck (2017); Sousa et al. (2018) for HD 106252; Santos et al. (2013) for HD 106515A and HD 106515B; Brewer et al. (2016) for HD 171238; Valenti & Fischer (2005); Bond et al. (2006); Santos et al. (2013) for HD 196067 and HD 196068; and Valenti & Fischer (2005); Bond et al. (2006); Sousa et al. (2006, 2008); Tsantaki et al. (2013); Jofré et al. (2015); Maldonado & Villaver (2016); Soto & Jenkins (2018) for HD 221420.

[c] The stellar masses are estimated from PARSEC isochrones (see text).

[d] The stellar luminosities are computed based on the absolute calibration of effective temperature scales performed by (Casagrande et al. 2010) (see text).

[e] The stellar ages and their 1σ error bars are approximated using the Bayesian technique of Brandt et al. (2014).

Our sample of targets comprises nine dwarf stars of G and early K spectral types, all of which have long term RV monitoring and precision spectroscopy. These stars have precise RV time series because their stable atmospheres and rich absorption spectra make them ideal targets for RV surveys: G and K stars constitute the majority of the host stars of RV-detected planets (Lineweaver & Grether 2003). In this Section, we provide a general overview on the photometric and atmospheric properties of the host stars using values from the literature. We then derive our own constraints on the ages and masses of our host stars. We need stellar masses in particular to infer planet masses from RV time series: the RV semi-amplitude is a function of both companion mass and total system mass.

To derive stellar masses, we first perform a uniform re-analysis on the stellar ages with an activity-based Bayesian method employing the stars' rotation and chromospheric activity (Brandt et al. 2014). Next, we estimate bolometric luminosities from Tycho-2 and 2MASS photometry using the absolutely calibrated effective temperature scale in Casagrande et al. (2010), and use metallicities, bolometric luminosities and the inferred stellar ages to infer masses using the PARSEC isochrones (Bressan et al. 2012). We describe our approaches for stellar ages and masses in more detail in the following, and discuss the results for each star individually. Our mass posteriors will later serve as the input priors in our joint orbit analysis of RV and absolute astrometry.

2.1. *Activity-based Age Analysis*

Stellar magnetic activity is a term that encompasses a range of phenomena observed of a star, including flares, star spots, and any chromospheric and coronal activity. Mid-F type and cooler main-sequence stars experience a decline in magnetic activity levels and rotational velocity as they age. The well-accepted explanation for the weaker activity and the slower rotation rates of old stars is the dynamo theory developed by Schatzman (1962); Schatzman (1990); Parker (1955, 1979): late-type stars develop subsurface convection zones that support a magnetic dynamo. The dynamo provides the energy to heat the stellar chromosphere and corona (Kraft 1967; Hall 2008; Testa et al. 2015, and references therein). The chromospheres eject winds in the form of jets or flares. These rotate with the stellar angular velocity out to the Alfvén radius, carrying away angular momentum which in turn causes the star to spin down over time. This effect is known as magnetic braking through the magnetic dynamo process (Noyes et al. 1984). The declining rotational velocity due to magnetic braking results in a reduction in the magnetic field generated by the stellar dynamo which, in turn, diminishes the star's Ca II HK and X-ray emissions. Ca II HK and X-ray emission weaken fastest at young ages, thus age dating for young stars is easier than for their old field star counterparts (Soderblom 2010).

Ca II HK emission, via the chromospheric activity index $R'_{\rm HK}$, has been widely used as an age indicator for Solar-type (G and K) stars. Age dating of Sun-like stars with $R'_{\rm HK}$ was first done by Wilson (1968) at the Mount Wilson Observatory. The age-activity relationship has since been developed and calibrated across spectral types later than mid-F (Skumanich 1972; Noyes et al. 1984; Soderblom et al. 1991; Barnes 2007; Mamajek & Hillenbrand 2008; David & Hillenbrand 2015; Angus et al. 2015; van Saders et al. 2016; Lorenzo-Oliveira et al. 2016). Conventionally, $R'_{\rm HK}$ is calculated from the Ca II S-index, a measurement of the strength of the emission. Mamajek & Hillenbrand (2008) calibrated the activity relations to an activity level of $\log R'_{\rm HK} \geq -5.0$ dex or a Rossby number (ratio of rotation period to convective overturn time) of 2.2, roughly corresponding to the Solar activity and rotation.

X-ray activity traces magnetic heating of the stellar corona, providing another indirect probe of rotation (Golub 1996; Mewe 1996; Jardine et al. 2002; Güdel 2004; Zhuleku et al. 2020). Brandt et al. (2014) combine $R'_{\rm HK}$ and X-ray activity to infer a Rossby number and, from this, an age via gyrochronology using the Mamajek & Hillenbrand (2008) calibration. Brandt et al. (2014) further allows for a distribution of times, dependent on spectral type, on the C-sequence where the dynamo is saturated and magnetic braking is inefficient (Barnes 2003). Their model sets a floor for the Rossby number at > 2.2, inflates the error in the activity and rotation by 0.06 dex to account for systematic uncertainties.

A photometric rotation period provides a more direct measure of the Rossby number and a tighter constraint on the stellar age. For stars that have directly measured rotation periods, Brandt et al. (2014) combine this measurement with the indirect probes of coronal and chromospheric emission to derive an age posterior. We refer the reader to that paper for a more detailed discussion.

We adopt the Bayesian inference model described in Brandt et al. (2014) to estimate stellar ages. We take the Ca II HK S-indices from the catalog of Pace (2013) and references therein and convert them to Mt. Wilson $R'_{\rm HK}$ using the relations described in (Noyes et al. 1984). We extract X-ray activities R_X from the ROSAT all-sky survey bright and faint source catalogs (Voges et al. 1999, 2000). For stars that are not in either ROSAT catalog, we take the nearest detection in the faint source

catalog and use five times its uncertainty as our upper limit on X-ray flux.

2.2. *Stellar Luminosity Analysis*

Here, we describe the method we use to estimate the bolometric luminosity for our sample of host stars. We adopt the absolutely calibrated effective temperature scales in Casagrande et al. (2010) for FGK stars across a wide range of metallicities. These authors use the InfraRed Flux Method (IRFM) to derive model independent effective temperatures $T_{\rm eff}$ in stars with different spectral types and metallicities. The homogeneous, all-sky Tycho-2 (B_T, V_T) optical photometry (Høg et al. 2000) was combined with the 2MASS infrared photometry in the JHK_s bands (Skrutskie et al. 2006) to calibrate reliable $T_{\rm eff}$ for a sample of solar analogs via IRFM.

All of our stars are late G and K sun-like dwarfs with optical and infrared photometry from Tycho-2 $(BV)_T$ and 2MASS JHK_s, thus we use Table 5 of Casagrande et al. (2010) to derive their bolometric integrated fluxes. In Table 5, the set of Tycho-2 and 2MASS flux calibrations apply to a [Fe/H] range between -2.7 and 0.4, and a color range between 0.19 and 3.29. The standard deviation σ_{ϕ_ξ} in the Tycho-2 and 2MASS flux calibrations is the smallest for the $m_\xi = V_T$ flux calibrations with color indices $V_T - J$ (0.7%) and $V_T - K_s$ (0.9%). We use the $V_T - J$ colors to calibrate V_T magnitudes for our sample of stars with the exception of HD 221420, which has a large uncertainty in its 2MASS J band magnitude due to saturation (4.997 ± 0.252 mag). Therefore, for HD 221420, we use the $V_T - K_s$ index instead to calculate the flux calibration in its V_T.

The final bolometric magnitudes can be estimated in terms of the V_T magnitude, the distance d, and the the integrated bolometric fluxes $\mathcal{F}_{\rm Bol}$(Earth):

$$L_{Bol} = 4\pi d^2 10^{-0.4V_T} \mathcal{F}_{\rm Bol}({\rm Earth}) \tag{1}$$

We express $L_{\rm Bol}$ in units of solar luminosity, adopting a value of $L_\odot = 3.828 \times 10^{33}$erg/s. Our parallaxes all have fractional uncertainties $\sim 10^{-3}$; they contribute negligibly to our luminosity uncertainties.

We propagate the errors using standard error propagation techniques. We estimate the final uncertainty in the luminosities as

$$\frac{\sigma^2(L_{\rm Bol})}{L_{\rm Bol}^2} = \left(\frac{\sigma(\mathcal{F}_{Bol})}{\mathcal{F}_{Bol}}\right)^2 + \left(\frac{2\sigma(\varpi)}{\varpi}\right)^2 + (0.4\ln(10)\sigma(V_T))^2 + (\sigma_{\phi_\xi})^2 \tag{2}$$

where the uncertainty in the flux calibration is σ_{ϕ_ξ} is 0.9% for HD 221420 and 0.7% for the rest of the sample. We summarize in Table 1 the Tycho-2 $(BV)_T$ and the 2MASS JHK_s photometry and our derived luminosity values for the host stars that we study.

2.3. *Stellar Masses and Metallicities*

We infer masses for all of our stars using the PARSEC isochrones (Bressan et al. 2012) by matching the observed luminosity at the spectroscopic metallicity and activity-based age.

We take spectroscopic metallicities from the PASTEL catalog (Soubiran et al. 2016, and references therein). The PASTEL catalog is a large compilation of high-dispersion spectroscopic measurements from the literature. For the metallicities, we take the median of all entries in the PASTEL catalog. We estimate the uncertainty in the metallicity as the standard deviation of the measurements in the PASTEL catalog, multiplied by $\sqrt{n/(n-1)}$ to correct for the bias in the estimator. Three targets—HD 171238, HD 29021, and HD 106515 A—have only single entries in the PASTEL catalog. For these stars we use the single measurement and assume a conservative uncertainty of 0.1 dex.

Once we have a probability distribution for metallicity, we take a fine grid of stellar models and, for each, compute a likelihood using

$$\mathcal{L} = p(\tau_{\rm model}) \times \exp\left[-\frac{(L_\star - L_{\rm model})^2}{2\sigma_L^2} - \frac{([{\rm Fe/H}]_\star - [{\rm Fe/H}]_{\rm model})^2}{2\sigma_{[{\rm Fe/H}]}^2}\right]. \tag{3}$$

In Equation (3), $p(\tau_{\rm model})$ is our activity-based age posterior at the model age. We then marginalize over metallicity and age to derive a likelihood as a function of stellar mass. We report the mean and standard deviation of this likelihood in Table 1 as $M_\star$(model) and adopt it as our (Gaussian) prior for orbital fits. The variances of these distributions are all small; weighting by an initial mass function has a negligible effect.

2.4. *Results on individual stars*

Here, we describe the results of the activity-based age analysis and the background for each individual star in our sample. The stellar distances we refer to in this section are inferred from *Gaia* EDR3 parallaxes. The fractional uncertainties on parallax are all $\lesssim$0.1%, so we simply take distance as the inverse of the parallax. The adopted stellar parameters in this paper, including Tycho-2 (Høg et al. 2000) and 2MASS (Cutri et al. 2003) photometry, $R'_{\rm HK}$, and R_X, are summarized in Table 1.

We combine the chromospheric index $R'_{\rm HK}$, the X-ray activity index R_X, and in some cases a photometric ro-

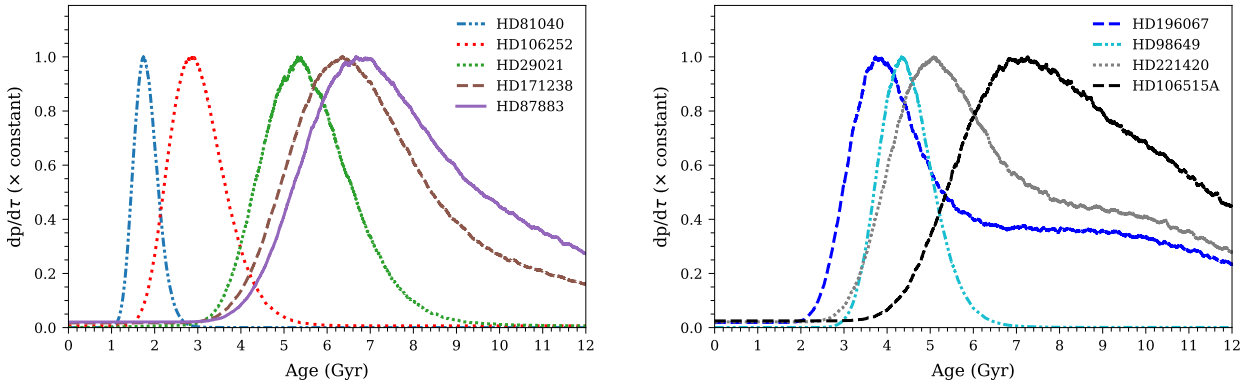

Figure 1. Normalized age posteriors for the nine stars presented in this work following the Bayesian technique of Brandt et al. (2014). This method combines the X-ray (R_X) and chromospheric activity ($R'_{\rm HK}$) indicators with an optional rotation period to constrain the Rossby number. It is then transformed into an age diagnostic for a specific star based on the calibration of Mamajek & Hillenbrand (2008).

tation period, to derive an age posterior for each star. Figure 1 shows the activity-based age posteriors for the whole sample of stars.

2.4.1. *HD 29021 (HIP 21571)*

HD 29021 is a G5 star located at a distance of 30.9 pc. Rey et al. (2017) estimated the stellar activity level of the star using high-resolution spectra obtained with the SOPHIE spectrograph at the 1.93 m telescope of the Haute-Provence Observatory, and no significant variability of the star was found from the $H\alpha$ activity indicator. The age of HD 29021 is determined to be ≈6 Gyr from our activity-based analysis, slightly lower than 7.4 Gyr from Winter et al. (2020), the only age reported for this star in the literature. We obtain a luminosity of $0.659 \pm 0.008\,L_\odot$, consistent with the luminosity of $\approx 0.7\,L_\odot$ from Anderson & Francis (2012); Gaia Collaboration et al. (2018). The mass estimate of the star is between 0.85-1.0 $M_\odot$ from multiple sources (Chandler et al. 2016; Mints & Hekker 2017; Goda & Matsuo 2019). Combining our luminosity and age with our adopted metallicity, we infer a mass of $0.86 \pm 0.02\,M_\odot$.

2.4.2. *HD 81040 (HIP 46076)*

HD 81040 is a bright, nearby, early G-dwarf star, commonly classified as a very young Galactic disc star (Montes et al. 2001). Sozzetti et al. (2006) used Ca II HK lines in the Keck/HIRES spectra to determine a chromospheric age of 0.73 ± 0.1 Gyr. A significant Lithium (Li) abundance of $\log \epsilon(Li) = 1.91 \pm 0.07$ also suggests youth (Sozzetti et al. 2006; Gonzalez et al. 2010). Oelkers et al. (2018) and Reinhold & Hekker (2020) measured rotation periods of 15.26 and 15.98 days, respectively, about half the Solar period. Our activity-based analysis produces a narrow age posterior centered just under 2 Gyr, slightly older than the Sozzetti et al. (2006) age. The mass of the star is consistently inferred to be between $0.93\,M_\odot$ and $1.01\,M_\odot$ (Sousa et al. 2006; Butler et al. 2006; Goda & Matsuo 2019). We obtain a mass of $0.99 \pm 0.02\,M_\odot$ from PARSEC isochrones.

2.4.3. *HD 87883 (HIP 49699)*

HD 87883 is a K star at a distance of 18.3 pc. Fischer et al. (2009) found modest chromospheric activity with $\log R'_{\rm HK} = -4.86$ dex, a stellar luminosity of $0.318 \pm 0.018\,L_\odot$, and a stellar jitter of $4.5\,{\rm m\,s^{-1}}$. We have adopted a slightly lower $\log R'_{\rm HK}$ value of -4.98 dex computed using S-indices from Strassmeier et al. (2000); Gray et al. (2003); Isaacson & Fischer (2010). We derive a slightly higher luminosity of $0.338 \pm 0.004\,L_\odot$. Literature estimates of the stellar mass range from 0.78–$0.85\,M_\odot$ (Valenti & Fischer 2005; Howard et al. 2010; Luck 2017; Santos et al. 2017; Anders et al. 2019; Maldonado et al. 2019; Stassun et al. 2019). We find a stellar mass from PARSEC isochrones of $0.80 \pm 0.02\,M_\odot$, in good agreement with previous results. Several studies have constrained the age of this star to ∼5–10 Gyr (Valenti & Fischer 2005; Takeda et al. 2007; Bonfanti et al. 2015; Brewer et al. 2016; Bonfanti et al. 2016; Yee et al. 2017; Luck 2017; Winter et al. 2020). Our adopted parameters combined produce an activity-based age peak at ≈7 Gyr which falls within that age range. The combined properties paint a picture of an old aged main-sequence K star with low to modest chromospheric and coronal activity levels.

2.4.4. *HD 98649 (HIP 55409)*

HD 98649, located at a distance of 42.2 pc from the Sun, is a G3/G5V dwarf. Porto de Mello et al. (2014) label it as a solar analog candidate that closely matches the Sun in colors, absolute magnitude, chromospheric

activity as measured from the $H\alpha$ indicator, and atmospheric characteristics. Our luminosity from Tycho-2 and 2MASS photometry yield $L_* = 0.968 \pm 0.012\,L_\odot$. Pace (2013) and Gáspár et al. (2016) have determined the age of the star to be between 4-5 Gyr, in agreement with our activity-based age of $4.436^{+0.677}_{-0.576}$ Gyr.

We adopt an activity index of $R'_{\rm HK} = -4.96$ using S-indices from Arriagada (2011); Jenkins et al. (2011); Pace (2013), consistent with the values published in many sources (Jenkins et al. 2008, 2011; Herrero et al. 2012; Marmier et al. 2013; Gondoin 2020). The spectroscopic mass of the star is between 0.96-1.03 $M_\odot$ (Allende Prieto & Lambert 1999; Mortier et al. 2013; Santos et al. 2013; Mints & Hekker 2017; Goda & Matsuo 2019). Our PARSEC isochrone fitting provides a value of $0.97 \pm 0.02\,M_\odot$ that is consistent with the literature values. The stellar rotation period is 26.44 days (Oelkers et al. 2018), again a close match to the Solar period. Based on the ≈4 Gyr peak from our activity-based analysis, HD 98649 is a chromospherically inactive G dwarf and a close Solar analog.

2.4.5. *HD 106252 (HIP 59610)*

HD 106252, at a distance of 38.1 pc, is a Sun-like G type star (González Hernández et al. 2010; Datson et al. 2012). Its chromospheric index is comparable with that of the Sun at the minimum of the solar cycle (Lanza et al. 2018). A weak lithium absorption feature (Perrier et al. 2003) and a $R'_{\rm HK} = -4.85$ from Pace (2013) indicate low stellar activity and an old age for HD 106252. Literature values agree on an age of ∼4.5 - 7.5 Gyr (Marsakov & Shevelev 1995; Gonzalez et al. 2010; Casagrande et al. 2011; Gontcharov 2012; Pace 2013; Bonfanti et al. 2016; Aguilera-Gómez et al. 2018). Our activity-based age indicators however favor a somewhat younger age, with our distribution peaking at ∼3 Gyr; this is driven by a single relatively active measurement by White et al. (2007). The stellar luminosity we infer is higher than that of the Sun. The mass of HD 106252 derived from the PARSEC isochrones model is $1.05 \pm 0.02\,M_\odot$, in agreement with independent determinations (Fischer & Valenti 2005; Butler et al. 2006; Marchi 2007; Goda & Matsuo 2019).

2.4.6. *HD 106515A (HIP 59743A)*

HD 106515 is a high common proper motion binary system consisting of the G-type stars HD 106515 A and B, with $V = 7.96$ and $V = 8.22$ mag, respectively. HD 106515 AB is a gravitationally bound system; the presence of the stellar companion HD 106515 B perturbs the orbit of the planet orbiting around HD 106515 A (Rica et al. 2017). HD 106515 B has an estimated spectroscopic mass of $0.925\,M_\odot$ and an effective temperature of 5425 K (Mugrauer 2019). Dommanget & Nys (2002) list a third visual stellar companion 98.″7 from HD 106515 A with a magnitude of $V = 10.3$ (BD-06 3533, or TYC 4946-202-1). *Gaia* EDR3 places this star at a distance of nearly 1 kpc, conclusively identifying it as a chance alignment.

HD 106515 A has a slow rotational velocity and low levels of chromospheric activity, with $R'_{\rm HK} = -5.10$ (Schröder et al. 2009; Meunier & Lagrange 2019), suggesting an old star. Our activity-based age analysis results in a broad posterior peaking at an age just under 8 Gyr. Previous mass measurements of HD 106515 A range between 0.87-0.95 $M_\odot$ (Allende Prieto & Lambert 1999; Santos et al. 2017; Anders et al. 2019; Goda & Matsuo 2019; Queiroz et al. 2020; Gomes da Silva et al. 2021). Our PARSEC isochrone fitting yields a mass of $0.90 \pm 0.03\,M_\odot$. We use the same method to derive a mass of $0.89 \pm 0.03\,M_\odot$ for HD 106515 B.

2.4.7. *HD 171238 (HIP 91085)*

HD 171238 is a G8 dwarf at a distance of 44.5 pc. With theoretical isochrones, Ségransan et al. (2010) obtain a mass of $M_* = 0.94 \pm 0.03\,M_\odot$ and an age of 4.9 ± 4.1 Gyr. Bonfanti et al. (2016) studied the age consistency between exoplanet hosts and field stars with the PARSEC evolutionary code, and found a stellar age of 4 ± 1.2 Gyr. Our activity-based age analysis yields a broad posterior spread of 3-12 Gyr with a peak at 6 Gyr, in mild tension with above mentioned values. The discrepancies in the ages and a broad posterior suggest that the age of the star is poorly constrained. Bonfanti et al. (2016) Bonfanti et al. (2016).

2.4.8. *HD 196067 (HIP 102125)*

HD 196067 is in a bright visual binary gravitationally bound to the G-dwarf star HD 196068 (=HIP 102128) (Gould & Chaname 2004). The binary pair is located 39.94 pc from the Sun. HD 196067 appears to be slightly evolved on the color-magnitude diagram. Marmier et al. (2013) derived an age of 3.3 ± 0.6 Gyr and a mass $M_* = 1.29 \pm 0.08 M_\odot$, with $[{\rm Fe/H}] = 0.34 \pm 0.04$. Our activity-based age for HD 196067 peaks at ≈4 Gyr, consistent with literature findings that most strongly favor an age of about 3 Gyr (Casagrande et al. 2011; Delgado Mena et al. 2015; Winter et al. 2020). These same authors as well as Valenti & Fischer (2005); Mortier et al. (2013); Santos et al. (2017); Goda & Matsuo (2019); Maldonado et al. (2019) infer masses between 1.23-1.32 $M_\odot$. The PARSEC isochrones yield a mass of $1.26 \pm 0.07\,M_\odot$, which agrees well with literature values. We derive a mass of $1.12 \pm 0.06\,M_\odot$ for its companion, HD 196068.

2.4.9. *HD 221420 (HIP 116250)*

HD 221420 is a slightly evolved G dwarf located 31.2 pc from the Sun. Holmberg et al. (2009) derive a photometric metallicity of [Fe/H] = 0.19 and an age of ∼5 Gyr. Spectroscopic measurements suggest an even higher metallicity (e.g. Valenti & Fischer 2005; Sousa et al. 2006; Tsantaki et al. 2013). Other authors have inferred ages between 4 and 6 Gyr (Valenti & Fischer 2005; Baumann et al. 2010; Casagrande et al. 2011; Pace 2013; Tsantaki et al. 2013; Aguilera-Gómez et al. 2018). Our activity-based age analysis yields an age posterior centered between 4-6 Gyr that closely matches the literature measurements. Unlike most of our other stars, HD 221420 has a luminosity and surface gravity that place it above the main sequence. We therefore verify the activity-based age with an analysis using only the observed luminosity combined with the PARSEC isochrones (Bressan et al. 2012). We derive an age of 3 to 5 Gyr with this approach, consistent with our activity-based age but excluding the tail to old ages.

We derive a mass of $1.28 \pm 0.08\,M_\odot$ using an activity-based age prior. This increases slightly to $1.35 \pm 0.09\,M_\odot$ if we use a uniform age prior. We adopt $1.28 \pm 0.08\,M_\odot$ for our analysis here. Using the higher mass would result in a slightly longer inferred orbital period and higher mass of the substellar companion.

3. RADIAL VELOCITY DATA

The RV time series for the stars come from decades of monitoring by several long-term RV surveys. Four of the targets, HD 171238 b, HD 98649 b, HD 196067 b and HD 106515 Ab, are long period and massive planets from the CORALIE survey (Marmier et al. 2013). HD 221420 b is a massive companion reported in Kane et al. (2019) with radial velocities from the 3.9-meter Anglo-Australian Telescope (AAT) in the course of the Anglo-Australian Planet Search (AAPS; Diego et al. 1990). It was also observed with the High Accuracy Radial velocity Planet Searcher (HARPS) spectrograph at the ESO 3.6-m telescope in La Silla (Trifonov et al. 2020). The rest of the sample have multi-decade RV data acquired with the HIRES instrument on the Keck I Telescope, the Hamilton spectrograph at Lick Observatory, and the ELODIE and SOPHIE spectrographs at Haute-Provence Observatory. In this section, we briefly summarize the long-term RV history for each star and the data we use for orbital fits.

3.1. *HD 29021 b*

HD 29021 was observed with SOPHIE+ survey for giant planets with 66 RV measurements on a 4.5 yr time baseline (Rey et al. 2017). The resulting orbital solution yielded a mass of $M \sin i = 2.4\,M_{\rm Jup}$ and an orbital period of 3.7 years, placing the planet just outside the outer limit of its star's habitable zone. The dispersion of the residuals from this fit is within the expected levels for SOPHIE+ and no long term drift was observed by these authors. We use all of the 66 RVs from the SOPHIE search for northern exoplanets.

3.2. *HD 81040 b*

Sozzetti et al. (2006) reported the detection of a massive planetary companion orbiting the young disc star HD 81040 based on five years of precise RV measurements with the HIRES spectrograph on the 10-m Keck telescope and the ELODIE fiber-fed echelle spectrograph on the 1.93 m telescope at the Observatoire de Haute-Provence in France. HIRES/Keck monitored this star for 8.5 months in 1991, obtaining a total of 3 RV measurements, and 23 follow-up RV data were taken with the ELODIE spectrograph from 2002-2005. The orbital fit to all of the data unveiled a massive planet with period $P = 1001.7 \pm 7.0$ days, $e = 0.526 \pm 0.042$ and $M \sin i = 6.86 \pm 0.71\,M_{\rm Jup}$ (Sozzetti et al. 2006). We utilize the combined data from ELODIE and HIRES/Keck for our orbit analysis.

3.3. *HD 87883 b*

The RV monitoring of HD 87883 began in 1998 December at Lick (Fischer et al. 2013). A total of 44 RV measurements with Lick have a median uncertainty of $5.3\,{\rm m\,s^{-1}}$. An additional 25 higher-quality RV measurements with the HIRES instrument in 2009 on the Keck telescope have a median precision of $4.0\,{\rm m\,s^{-1}}$ (Fischer et al. 2009). A Keplerian fit to RV data from both Lick and Keck revealed a single long-period RV companion with a period of 7.55 ± 0.24 years, an eccentricity of 0.53 ± 0.12 and a minimum mass of $M \sin i = 1.78 \pm 0.13\,M_{\rm Jup}$ (Fischer et al. 2009). Butler et al. (2017) has published an additional 46 RVs with a median uncertainty of $1.35\,{\rm m\,s^{-1}}$ (Butler et al. 2017) that extends the total time baseline to more than 20 years. We use all of the above measurements in our orbit analysis.

3.4. *HD 98649 b*

For HD 98649, a total of 11 radial velocity measurements were published from CORALIE-98 with a median measurement uncertainty of $4.4\,{\rm m\,s^{-1}}$. Then, 37 data were published from CORALIE-07 with a median error of $3.3\,{\rm m\,s^{-1}}$. Using the combined data, Marmier et al. (2013) uncovered a companion with $M \sin i = 6.8\,M_{\rm Jup}$, a period of $13.6^{+1.6}_{-1.3}$ years on an eccentric orbit with $e = 0.85$. CORALIE measured 15 additional RVs in 2014. We make use of all of the 70 RV measurements

acquired with the CORALIE spectrograph in the 16-year time span.

3.5. *HD 106252 b*

HD 106252 was observed with the ELODIE high-precision echelle spectrograph at Haute-Provence Observatory as part of the ELODIE survey for northern extra-solar planets (Perrier et al. 2003). A total of 40 high-precision RV measurements with a median uncertainty of 10.5 $\mathrm{m\,s^{-1}}$ were obtained since March 1997 (Perrier et al. 2003). Using these data, Perrier et al. (2003) performed orbit analysis for the companion and found a well-constrained solution with minimum mass of $M \sin i \approx 7.56\,M_{\rm Jup}$, an eccentricity of 0.471 ± 0.028, and a period of 4.38 ± 0.05 years. Fischer et al. (2002) independently confirmed the planet using 15 RV measurements (median uncertainty of 11 $\mathrm{m\,s^{-1}}$) from Hamilton/Lick, but with poorer constrains due to shorter temporal coverage Perrier et al. (2003). We use both the 40 RVs from ELODIE and 15 measurements from Hamilton.

HD 106252 was observed again with both ELODIE and Hamilton after the initial publications in 2002/2003, providing an additional 15 RVs from ELODIE with a median uncertainty of 11.1 $\mathrm{m\,s^{-1}}$, and 54 RVs from Hamilton with median errors of 10.5 $\mathrm{m\,s^{-1}}$ in 2006 (Butler et al. 2006). We also use the most recent RV measurements in 2009 that include 12 RVs from CDES-TS2 (median uncertainty 10.35 $\mathrm{m\,s^{-1}}$) and 43 RVs (median uncertainty 9.3 $\mathrm{m\,s^{-1}}$) from the High Resolution Spectrograph (HRS) instrument mounted on the 9.2 m Hobby-Eberly Telescope (HET) at the McDonald Observatory (Wittenmyer et al. 2016). Altogether, we use 179 RV data points spanning 12 years.

3.6. *HD 106515 Ab*

In the same CORALIE survey, a massive planet HD 106515 Ab was discovered around one star in the binary system HD 106515 (Marmier et al. 2013). A total of 19 and 24 RV measurements have been collected with CORALIE-98 and CORALIE-07 with median measurement uncertainties of 6.3 $\mathrm{m\,s^{-1}}$ and 4.1 $\mathrm{m\,s^{-1}}$, respectively (Marmier et al. 2013). Its orbital parameters are well constrained, with $M \sin i = 9.61 \pm 0.14\,M_{\rm Jup}$, $P = 3630 \pm 12$ days, $e = 0.572 \pm 0.011$, and a semi-major axis of 4.590 ± 0.010 AU. Similar to HD 196067, with the presence of a stellar companion, the Kozai-Lidov pumping mechanism (Kozai 1962; Lidov 1962) may be a viable explanation for the high eccentricity. We use all the CORALIE RVs.

3.7. *HD 171238 b*

The RV monitoring of HD 171238 started in October 2002 using the CORALIE spectrograph mounted on the 1.2 Euler Swiss telescope at La Silla Observatory in Chile (Ségransan et al. 2010). Those authors published 32 RV measurements from CORALIE-98 with a median measurement uncertainty of 7.3 $\mathrm{m\,s^{-1}}$. An additional 65 RV measurements from CORALIE-07 show a median measurement error of 3.7 $\mathrm{m\,s^{-1}}$. Using these radial velocities, Ségransan et al. (2010) reported a massive companion with $M \sin i = 2.60\,M_{\rm Jup}$, a period of 4.17 yrs, a semi-major axis of 2.5 AU, and an eccentricity of $e = 0.40$. They also speculate that the presence of spots on the stellar surface and active chromospheric activity might be the cause of the large RV jitter (10 $\mathrm{m\,s^{-1}}$) from their single planet Keplerian model fitting. We adopt the 32 RVs from CORALIE-98, 65 RVs from CORALIE-07 and an additional 9 RVs published in 2017 with the HIRES spectrograph on the Keck Telescope (Butler et al. 2017).

3.8. *HD 196067 b*

Like HD 98649 b, HD 196067 b was also discovered in the CORALIE survey for southern exoplanets. A total of 82 Doppler measurements have been obtained since September 1999: 30 were from CORALIE-98 with a median measurement uncertainty of 7.5 $\mathrm{m\,s^{-1}}$ and 52 from CORALIE-07 with a median uncertainty of 5.9 $\mathrm{m\,s^{-1}}$ (Marmier et al. 2013). The data for C98 are sparsely sampled due to poor coverage near periastron (Marmier et al. 2013). With the caveats from this poor coverage, the companion's $M \sin i$ is constrained between $5.8 - 10.8 M_{\rm Jup}$, the period between 9.5-10.6 yr, and the eccentricity between 0.57-0.84. We use the RVs from both CORALIE-98 and CORALIE-07.

3.9. *HD 221420 b*

The companion to HD 221420 was discovered by Kane et al. (2019) using 18 years of RV data acquired with the Anglo-Australian Telescope (AAT) (AAPS; Diego et al. 1990). The median uncertainty of the 88 measurements is 1.33 $\mathrm{m\,s^{-1}}$. Kane et al. (2019) obtain an orbital period of $61.55^{+11.50}_{-11.23}$ years, a RV semi-amplitude of $54.7^{+4.2}_{-3.6}$, an eccentricity of $0.42^{+0.05}_{-0.07}$, and a $M \sin i$ of $9.7^{+1.1}_{-1.0}\,M_{\rm Jup}$; they infer a semi-major axis of 18.5 ± 2.3 AU. The High Accuracy Radial velocity Planet Searcher (HARPS) spectrograph (ESO) also observed the target from 2003-2015, offering 74 higher precision measurements with a median uncertainty of 0.94 $\mathrm{m\,s^{-1}}$. Both AAT+HARPS data are recently utilized by Venner et al. (2021) to derive a precise dynamical mass of $22.9 \pm 2.2 M_{\rm Jup}$. We include all the RV measurements from AAT and HARPS for this target.

Table 2. Summary of Hipparcos and Gaia (EDR3) Astrometry from HGCA.[a]

Star	Data Source	$\mu_{x,\alpha*}$ mas yr^{-1}	$\sigma[\mu_{\alpha*}]$	$\mu_{x,\delta}$ mas yr^{-1}	$\sigma[\mu_\delta]$	Correlation Coefficient	Epoch, α year	Epoch, δ	$\Delta\mu_{x-HG,\alpha*}$ mas yr^{-1}	$\Delta\mu_{x-HG,\delta}$	Significance
HD 29021	Hip	60.884	0.674	22.917	0.717	0.160	1991.11	1990.92	-1.004 ± 0.674	-0.261 ± 0.717	
	HG	61.888	0.020	23.178	0.020	0.020					
	Gaia	62.078	0.025	23.430	0.025	0.266	2016.41	2016.09	0.190 ± 0.032	0.252 ± 0.032	8.89σ
HD 81040	Hip	−151.520	0.835	35.954	0.525	−0.320	1991.66	1991.34	-0.369 ± 0.836	0.190 ± 0.525	
	HG	−151.151	0.031	35.764	0.019	−0.265					
	Gaia	−151.265	0.061	35.708	0.049	−0.404	2016.11	2016.32	-0.114 ± 0.068	-0.056 ± 0.053	1.98σ
HD 87883	Hip	−64.197	0.665	−60.478	0.466	−0.006	1991.50	1991.09	-0.391 ± 0.665	0.113 ± 0.466	
	HG	−63.806	0.024	−60.591	0.017	−0.062					
	Gaia	−64.293	0.037	−61.438	0.035	−0.214	2016.13	2016.33	-0.487 ± 0.044	-0.847 ± 0.039	26.57σ
HD 98649	Hip	−199.571	0.663	−177.725	0.575	−0.432	1991.18	1991.51	-0.019 ± 0.663	-0.187 ± 0.575	
	HG	−199.552	0.024	−177.538	0.022	−0.478					
	Gaia	−199.735	0.031	−177.620	0.023	−0.047	2015.81	2015.84	-0.183 ± 0.039	-0.082 ± 0.032	5.68σ
HD 106252	Hip	23.781	0.886	−279.571	0.444	−0.068	1991.28	1991.42	0.179 ± 0.886	0.602 ± 0.444	
	HG	23.602	0.029	−280.173	0.017	−0.144					
	Gaia	23.315	0.044	−279.896	0.028	−0.409	2015.94	2015.49	-0.287 ± 0.053	0.277 ± 0.033	8.65σ
HD 106515A	Hip	−249.256	1.074	−53.466	0.875	−0.372	1991.39	1991.10	1.650 ± 1.075	-1.749 ± 0.876	
	HG	−250.906	0.048	−51.717	0.035	−0.318					
	Gaia	−251.469	0.043	−51.330	0.030	−0.317	2016.10	2016.10	-0.563 ± 0.064	0.387 ± 0.046	10.27σ
HD 171238	Hip	−30.814	1.549	−110.327	1.042	0.069	1991.04	1991.22	-1.776 ± 1.550	-0.713 ± 1.042	
	HG	−29.038	0.043	−109.614	0.030	−0.046					
	Gaia	−29.539	0.046	−109.580	0.038	0.258	2016.25	2016.55	-0.501 ± 0.063	0.034 ± 0.048	7.87σ
HD 196067	Hip	150.240	2.186	−159.708	2.343	−0.477	1991.31	1991.16	-5.894 ± 2.187	1.833 ± 2.344	
	HG	156.134	0.074	−161.541	0.079	−0.277					
	Gaia	156.404	0.026	−162.214	0.031	−0.298	2015.97	2016.24	0.270 ± 0.078	-0.673 ± 0.085	7.76σ
HD 221420	Hip	15.884	0.437	1.648	0.385	0.159	1991.14	1991.30	0.911 ± 0.437	1.193 ± 0.385	
	HG	14.973	0.014	0.455	0.012	0.042					
	Gaia	16.306	0.056	0.736	0.058	0.110	2016.06	2015.98	1.333 ± 0.058	0.281 ± 0.059	23.11σ

[a] from Brandt (2021)

4. ABSOLUTE STELLAR ASTROMETRY

Absolute astrometry of each of our host stars provides a constraint orthogonal to that from radial velocities. The ESA satellites *Hipparcos* and *Gaia* each measure a position and proper motion in an inertial reference frame (the International Celestial Reference Frame, or ICRF), but taken 25 years apart. *Hipparcos* detected proper motions near epoch 1991.25 (μ_{Hip}), and *Gaia* near 2016.0 ($\mu_{Gaia,EDR3}$). Differences between the two proper motions probe a star's acceleration. An additional, more accurate tangential proper motion is given by the *Hipparcos*-*Gaia* positional difference divided by the ∼25 year time baseline (μ_{HG}). We reference this scaled positional difference by subtracting it from both *Hipparcos* and *Gaia* proper motions ($\Delta\mu_{Hip-HG}$ or $\Delta\mu_{Gaia-HG}$), and we use them as astrometric constraints for the host stars' orbits. We report these variables in Table 2. The proper motion of a star in conjunction with its radial velocity define a three-dimensional vector that traces out the true space velocity of the star.

Table 2 summarizes the *Gaia* EDR3 version HGCA catalog astrometry for the host stars in our sample. While *Gaia* and *Hipparcos*'s measurements are independent, a slight covariance results from the use of *Gaia* parallaxes to improve the *Hipparcos* astrometry (Brandt 2018). We neglect this small covariance in our orbital fits.

All of our stars except for HD 81040 have acceleration χ^2 values greater than 11.8 (i.e., 3σ detections assuming Gaussian errors and two degrees of freedom), indicating significant accelerations between *Hipparcos* and *Gaia*.

5. SINGLE-EPOCH RELATIVE ASTROMETRY FOR 3-BODY FITTING

Among the stars in our sample, two systems have gravitationally bound, wide stellar companions measured independently in *Gaia* EDR3. These include HD 196067's stellar companion HD 196068, and HD 106515 A's secondary stellar companion HD 106515 B as discussed in Section 2. Table 3 lists the single epoch relative astrometry data for both of these systems here. This is obtained using the single epoch measurements of position in R.A. and Dec. (α, δ) from *Gaia* EDR3 at epoch 2016.0 and

Table 3. Adopted single epoch relative astrometry derived from Gaia EDR3.

Companion	HD 196068	HD 106515 B
Epoch	2016.0	2016.0
ρ ($''$)	16.62	6.86
σ_ρ ($''$)[a]	0.01	0.01
PA ($^\circ$)	19.3	85.9
$\sigma_{\rm PA}$ ($^\circ$)[a]	0.1	0.1
$\mu_{\rm Gaia,\alpha*}$ (mas yr^{-1})	163.531	−244.603
$\sigma[\mu_{\rm Gaia,\alpha*}]$ (mas yr^{-1})	0.016	0.031
$\mu_{\rm Gaia,\delta}$ (mas yr^{-1})	−171.346	−67.744
$\sigma[\mu_{\rm Gaia,\delta}]$ (mas yr^{-1})	0.018	0.021
Corr Coefficient	−0.156	−0.650
$\Delta\mu_{\rm comp-host,\alpha*}$ (mas yr^{-1})	7.127	6.866
$\sigma[\Delta\mu_{\rm comp-host,\alpha*}]$ (mas yr^{-1})	0.031	0.053
$\Delta\mu_{\rm comp-host,\delta}$ (mas yr^{-1})	-9.132	-16.414
$\sigma[\Delta\mu_{\rm comp-host,\delta}]$ (mas yr^{-1})	0.036	0.037

[a] Adopted errors are much larger than *Gaia* EDR3 values to aid MCMC convergence.

converting them into position angle east of north (PA) and projected separation (ρ) between the host star and the secondary stellar companion.

We adopt uncertainties of 10 mas in separation and 0.°1 in PA. These are much larger than the formal *Gaia* uncertainties, but still represent tiny fractional uncertainties. Adopting the actual formal *Gaia* uncertainties gives measurements so precise that it makes the MCMC chains much slower to converge.

Gaia EDR3 also gives proper motions for both stellar companions. We use these proper motions together with the relative astrometry to constrain the orbital fit. Both stellar companions are of similar brightness to the primary stars that we fit. As a result, the magnitude-dependent frame rotation seen by Cantat-Gaudin & Brandt (2021) will be shared by both components and will not affect our analysis.

We impose priors on the masses of the secondary star in both cases. We derive these from the same stellar isochrone fitting described in Section 2.2. For HD 106515 B we find a mass of $0.86 \pm 0.03\,M_\odot$. This value is slightly lower than $0.925 \pm 0.05\,M_\odot$ from Mugrauer (2019). For HD 196068, we adopt a prior of $1.18 \pm 0.06\,M_\odot$.

6. ORBITAL FIT

Precise masses and inclinations become possible for RV planets because RV and astrometry measure orthogonal components of the motion in inertial frames. We perform full orbital analyses for our sample of RV planets using the orbit fitting package `orvara` (Brandt et al. 2021c). `orvara` fits Keplerian orbits to an arbitrary combination of radial velocity, relative and/or absolute astrometry data. None of the RV-detected companions in our sample have previous relative astrometry data from direct imaging. Three of these systems, HD 87883, HD 106252 and HD 106515 AB, were previously observed with AO imaging that did not show signs of companions in the systems. HD 87883 was observed with the Calar Alto 2.2-m telescope with the lucky imaging camera AstraLux in (Ginski et al. 2012; Luck 2017). HD 106252 was imaged with Palomar/Keck as part of the AO survey of young solar analogs in June, 2004 (Metchev & Hillenbrand 2009). Finally, the HD 106515 AB system was imaged with AdoPT@TNG (Desidera et al. 2012). For the present analysis, we use published RV data from the literature described in Section 3 and absolute astrometry data from the HGCA described in Section 4.

`orvara` uses the intermediate astrometry fitting package `htof` (Brandt et al. 2021b). `htof` parses the intermediate *Hipparcos* astrometric data by accounting for the scan angles and uncertainties to construct covariance matrices to solve for best-fit positions and proper motion relative to the barycenter. The *Gaia* epoch astrometry is currently unavailable, so `htof` uses an approach to forward model *Gaia* observations using the predicted scan angles and observation times, and fits a five-parameter astrometric model to these synthetic data. The *Gaia* EDR3 predicted observation times and scan angles are publicly accessible via the *Gaia* Observation Forecast Tool [1]. `orvara` then compares the resulting positions and proper motions to the values provided in the HGCA.

`orvara` adopts the parallel-tempering Markov Chain Monte Carlo (MCMC) sampler with `ptemcee` (Foreman-Mackey et al. 2013; Vousden et al. 2016) to explore the 9-dimensional parameter space comprised of the host star and companion masses M_* and $M_{\rm sec}$, RV jitter, semi-major axis a, inclination i, PA of the ascending node Ω, mean longitude at a particular reference epoch of 2455197.5 JD (λ_{ref}), the eccentricity e and the argument of periastron (ω) fitted as $\sqrt{e}\sin\omega$ and $\sqrt{e}\cos\omega$. For our three-body systems, there are six more orbital elements plus another mass; these become 16-parameter fits.

In addition to the nine free parameters that we fit (sixteen for three-body systems), `orvara` marginalizes out several nuisance parameters to reduce computational costs. These include the systemic RV zero point (one per instrument), the parallax, and the barycenter proper

[1] https://gaia.esac.esa.int/gost/index.jsp

Table 4. Adopted Priors.

Parameter	Prior
RV Jitter $\sigma_{\rm jit}$	$1/\sigma_{\rm jit}$ (log-flat)
Primary Mass M_*	$1/M$ (Gaussian)
Secondary Mass $M_{\rm sec}$	$1/M$ (log-flat)
Semimajor axis a	$1/a$ (log-flat)
$\sqrt{\varepsilon}\sin\omega$	uniform
$\sqrt{\varepsilon}\cos\omega$	uniform
Inclination i	$\sin(i)$, $0^\circ < i < 180^\circ$ (geometric)
Mean longitude at 2010.0 $\lambda_{\rm ref}$	uniform
Ascending node Ω	uniform
Parallax ϖ	$\exp\left[-\frac{1}{2}(\varpi - \varpi_{\rm EDR3})^2/\sigma_\varpi^2\right]$

motion. We assume the *Gaia* EDR3 parallax as our parallax prior, and use flat priors for the RV zero point(s) and barycenter proper motion. `orvara` thus produces posterior distributions for all of these parameters as well.

We perform orbital fits for each RV companion in our sample with `orvara`. We chose informative priors on the host stars' masses according to stellar masses derived in Section 2 and listed in Table 1. These are Gaussian with the means and standard deviations given in Table 1. We assume uninformative priors for our other fitted parameters: either log-uniform, uniform, or geometric (see Table 4), except for parallax, which we have marginalized out from the fit. For each target, we use `ptemcee` to fit for the nine parameters, employing 30 temperatures and 100 walkers over 5×10^5 steps per walker. In each case, the MCMC chains converge after no more than 15,000 steps, we thus discard the first 20,000 steps as burn-in and use the rest for inference. We post-process the MCMC chains with `orvara`, and we discuss the results for each individual system in the following Section.

7. UPDATED ORBITAL PARAMETERS

Table 5. Posteriors of single RV companions in our sample from orvara MCMC analysis.

Companion	HD 29021 b	HD 81040 b	HD 87883 b	HD 98649 b	HD 106252 b	HD 106515 Ab	HD 106515 B*	HD 171238 b	HD 196067 b	HD 196068*	HD 221420 b
Fitted parameters											
RV Jitter σ ($\mathrm{m\,s^{-1}}$)	$3.66^{+0.60}_{-0.58}$	$4.14^{+0.69}_{-4.1}$	$4.92^{+0.06}_{-0.12}$	$4.74^{+0.19}_{-0.34}$	$2.9^{+1.7}_{-2.9}$	$7.6^{+1.3}_{-1.3}$	$7.6^{+1.3}_{-1.3}$	$4.96^{+0.03}_{-0.06}$	$7.7^{+1.2}_{-1.1}$	$7.7^{+1.2}_{-1.1}$	$3.75^{+0.25}_{-0.23}$
Primary Mass ($\mathrm{M_\odot}$)	0.86 ± 0.02	0.97 ± 0.02	0.80 ± 0.02	0.97 ± 0.02	1.05 ± 0.02	0.90 ± 0.03	0.90 ± 0.03	0.92 ± 0.03	1.34 ± 0.06	1.34 ± 0.06	1.30 ± 0.08
Secondary Mass ($\mathrm{M_{Jup}}$)	$4.47^{+0.67}_{-0.65}$	$7.24^{+1.0}_{-0.37}$	$6.31^{+0.31}_{-0.32}$	$9.7^{+2.3}_{-1.9}$	$10.00^{+0.78}_{-0.73}$	$18.9^{+1.5}_{-1.4}$	904^{+31}_{-31}	$8.8^{+3.6}_{-1.3}$	$12.5^{+2.5}_{-1.8}$	1235^{+58}_{-59}	$20.6^{+2.0}_{-1.6}$
Semimajor axis a (AU)	$2.294^{+0.019}_{-0.019}$	$1.946^{+0.014}_{-0.014}$	$3.77^{+0.12}_{-0.094}$	$5.97^{+0.24}_{-0.21}$	$2.655^{+0.017}_{-0.017}$	$4.48^{+0.050}_{-0.050}$	335^{+96}_{-42}	$2.518^{+0.032}_{-0.033}$	$5.10^{+0.22}_{-0.17}$	1701^{+206}_{-186}	$9.99^{+0.74}_{-0.70}$
$\sqrt{e}\,\sin\,\omega$	$-0.007^{+0.038}_{-0.039}$	$0.714^{+0.018}_{-0.020}$	$-0.831^{+0.019}_{-0.019}$	$-0.865^{+0.023}_{-0.012}$	$-0.645^{+0.010}_{-0.010}$	$0.625^{+0.019}_{-0.020}$	$0.39^{+0.16}_{-0.28}$	$0.437^{+0.024}_{-0.024}$	$0.426^{+0.056}_{-0.066}$	$0.839^{+0.028}_{-0.073}$	$-0.254^{+0.062}_{-0.063}$
$\sqrt{e}\,\cos\,\omega$	$-0.672^{+0.010}_{-0.010}$	$0.114^{+0.041}_{-0.041}$	$0.178^{+0.055}_{-0.055}$	$-0.312^{+0.051}_{-0.10}$	$0.253^{+0.016}_{-0.017}$	$-0.424^{+0.029}_{-0.029}$	$-0.54^{+0.41}_{-0.12}$	$0.408^{+0.038}_{-0.040}$	$-0.702^{+0.080}_{-0.13}$	$-0.20^{+0.16}_{-0.18}$	$-0.312^{+0.10}_{-0.071}$
Inclination ($i < 90°$) (°) [a]	$33.7^{+6.8}_{-4.9}$	73^{+12}_{-16}	$16.8^{+1.7}_{-1.4}$	$43.7^{+13}_{-8.1}$	$46.0^{+4.9}_{-4.1}$	$29.2^{+2.4}_{-2.2}$	$18.8^{+7.8}_{-8.3}$	$19.1^{+7.9}_{-8.5}$	$41.2^{+28}_{-9.1}$	$10.6^{+6.1}_{-5.2}$	$17.8^{+2.9}_{-2.8}$
Inclination ($i > 90°$) (°) [a]	$146.3^{+4.9}_{-6.8}$	107^{+16}_{-12}	$163.2^{+1.4}_{-1.7}$	$136.3^{+8.1}_{-13}$	$134.0^{+4.1}_{-4.9}$	$150.8^{+2.2}_{-2.4}$	–	$162.9^{+5.0}_{-3.1}$	$138.8^{+9.1}_{-28}$	–	$162.2^{+2.8}_{-2.9}$
Ascending node Ω (°)	$40.8^{+7.1}_{-9.1}$	77^{+27}_{-23}	$109.9^{+4.0}_{-4.1}$	54^{+44}_{-26}	$105.3^{+10}_{-6.1}$	$59.9^{+4.6}_{-4.1}$	62^{+45}_{-37}	71^{+47}_{-13}	101^{+59}_{-82}	163^{+12}_{-158}	$66.6^{+5.4}_{-3.1}$
Mean longitude at λ_{ref} (°)	$15.2^{+2.7}_{-2.7}$	$148.3^{+3.7}_{-3.8}$	$73.7^{+13}_{-7.4}$	$75.8^{+4.1}_{-7.6}$	$174.6^{+1.5}_{-1.6}$	$100.5^{+1.8}_{-1.8}$	128^{+37}_{-110}	$59.0^{+3.0}_{-3.0}$	150^{+13}_{-15}	93^{+12}_{-11}	$170.5^{+2.3}_{-2.2}$
Derived parameters											
Period (years)	$3.737^{+0.018}_{-0.018}$	$2.7452^{+0.011}_{-0.0093}$	$8.23^{+0.32}_{-0.34}$	$14.74^{+0.88}_{-0.75}$	$4.202^{+0.011}_{-0.010}$	$9.927^{+0.030}_{-0.032}$	4630^{+2150}_{-850}	$4.148^{+0.045}_{-0.046}$	$9.88^{+0.63}_{-0.43}$	44300^{+8700}_{-7600}	$27.7^{+3.0}_{-2.5}$
Argument of periastron ω (°)	$180.6^{+3.4}_{-3.2}$	$81.0^{+3.3}_{-3.3}$	$282.1^{+3.7}_{-3.7}$	$250.2^{+3.2}_{-6.3}$	$291.4^{+1.5}_{-1.5}$	$124.1^{+2.6}_{-2.5}$	144^{+26}_{-42}	$46.9^{+3.9}_{-3.7}$	$148.6^{+7.6}_{-5.5}$	103^{+13}_{-11}	219^{+17}_{-12}
Eccentricity e	$0.453^{+0.014}_{-0.013}$	$0.525^{+0.024}_{-0.026}$	$0.720^{+0.038}_{-0.027}$	$0.852^{+0.033}_{-0.022}$	$0.480^{+0.010}_{-0.010}$	$0.571^{+0.012}_{-0.012}$	$0.399^{+0.12}_{-0.064}$	$0.358^{+0.028}_{-0.026}$	$0.70^{+0.14}_{-0.12}$	$0.744^{+0.024}_{-0.027}$	$0.162^{+0.035}_{-0.030}$
Semimajor axis (mas)	$74.29^{+0.61}_{-0.62}$	$56.55^{+0.41}_{-0.41}$	$206.4^{+6.7}_{-5.2}$	$141.6^{+5.7}_{-4.9}$	$69.68^{+0.45}_{-0.46}$	$131.2^{+1.5}_{-1.5}$	9813^{+2815}_{-1227}	$56.63^{+0.73}_{-0.74}$	$127.6^{+5.5}_{-4.2}$	42600^{+5200}_{-4700}	321^{+24}_{-23}
Periastron time (JD − 2450000)	$5824.8^{+9.4}_{-9.0}$	$5511.1^{+10}_{-8.7}$	6913^{+17}_{-16}	10500^{+330}_{-280}	$6463.0^{+8.4}_{-8.6}$	$5435.8^{+8.7}_{-8.5}$	$1570000^{+810000}_{-330000}$	5905^{+20}_{-20}	6560^{+350}_{-270}	485600^{+8500}_{-9700}	6580^{+430}_{-280}
$M_p \sin i$ (M_{Jup}) (this work)	$2.483^{+0.070}_{-0.068}$	$6.87^{+0.19}_{-0.19}$	$1.82^{+0.12}_{-0.10}$	$6.64^{+0.45}_{-0.23}$	$7.20^{+0.13}_{-0.13}$	$9.25^{+0.25}_{-0.25}$	–	$2.599^{+0.090}_{-0.088}$	$7.9^{+4.7}_{-1.5}$	–	$6.24^{+0.65}_{-0.59}$
$M_p \sin i$ (M_{Jup}) (literature)	$2.4^{+0.2}_{-0.2}$	$6.86^{+0.71}_{-0.71}$	$1.54^{+0.26}_{-0.26}$	$7.27^{+0.98}_{-0.98}$	$6.93^{+0.27}_{-0.27}$	$9.08^{+0.20}_{-0.20}$	–	$2.72^{+0.49}_{-0.49}$	$6.9^{+3.9}_{-1.1}$	–	$6.31^{+0.60}_{-0.61}$
Literature mass reference [b]	R17	S06 S17	S17 F09	R19 M13	S17 W09 L14	S19 M13	–	M18 S10	M13	–	V21 K19
Difference in $M_p \sin i$ (%)	3.3%	0.1%	15.4%	9.5%	3.8%	1.8%	–	4.7%	12.7%	–	1.1%
Difference in $M_p \sin i$ (σ)	0.39σ	0.01σ	1.01σ	0.63σ	0.90σ	0.53σ	–	0.24σ	0.54σ	–	0.08σ

* Secondary stellar companion. Their `orvara` masses in solar masses are $0.86 \pm 0.03\,M_\odot$ for HD 106515 B and $1.18 \pm 0.06\,M_\odot$ for HD 106515 B.

[a] The inclination distributions are usually bimodal, so we separately report the values for prograde and retrograde orbits.

[b] References abbreviated as S06 (Sozzetti et al. 2006); F09 (Fischer et al. 2009); W09 (Wittenmyer et al. 2009); S10 (Ségransan et al. 2010); M13 (Marmier et al. 2013); L14 (Liu et al. 2014); R17 (Rey et al. 2017); S17 (Stassun et al. 2017); M18 (Ment et al. 2018); V21 (Venner et al. 2021); K19 (Kane et al. 2019); R19 (Rickman et al. 2019); S19 (Saffe et al. 2019). Tabulated masses are from the first reference for each star. The other measurements are 1.78 ± 0.34 (F09) for HD 87883 b; 7.61 ± 0.39 (W09) and 6.92 ± 0.16 (L14) for HD 106252b; 2.60 ± 0.15 (S10) for HD 171238b; 7.27 ± 0.98 (S17) for HD 81040b; 6.8 ± 0.5 (M13) for HD 98649b; and $9.61^{+0.14}_{-0.14}$ (M13) for 106515 Ab.

In this section, we summarize the results of our orbital fits to each target. The `orvara` radial velocity fits and relative astrometric orbits are shown in Figure Set A1, and the corner plots and covariances of our orbital posteriors are showcased in Figure Set A10, both are presented in the appendix. Table 5 lists the nine basic Keplerian orbital elements `orvara` fit, and the inferred parameters computed using the fitted parameters, as well as the $M \sin i$ values from the literature. We obtain tight constraints on the masses of companions except for HD 171238. Aside from HD 221420 b, whose precise mass was measured by Venner et al. (2021), we present the first precise dynamical mass and orbital inclination measurements for the RV companions in our sample. Our derived $M \sin i$ values agree with the RV-only literature values to within 1σ.

For the inclinations (or equivalently the position angle of the ascending node Ω) derived in this paper, there are two complementary values whose absolute values wrap around 180°. This is unsurprising since the orbital inclination is dependent on whether the planet is in prograde ($0 \geq i_1 \leq 90$) or retrograde ($i_2 = 180° - i_1$) motion (Kervella et al. 2020), and there are limited ways to determine which orbit the companion is on without high contrast imaging. Unfortunately, besides the long-period brown dwarfs in our sample, none of the other companions are accessible to imaging in the near term.

The relative astrometric orbits of every RV companion with respect to its host star are demonstrated in Fig. 2. As a result of bimodal inclinations, the prograde and retrograde orbits are clearly evident from the two families of orbits shown in the plots.

The orbital fits to the RVs and absolute astrometry from HGCA are presented in Figure Set A1. The host stars' astrometric reflex motions over the 25-year time baseline between Hipparcos and Gaia are clearly seen. These figures show that the astrometric reflex motion of a star oscillates with a fixed period over 25 years, short period companions induce more cycles of oscillation. One of our companions, HD 221420 b, is a possible target for direct imaging. Figure 12 shows its predicted locations at four future dates. Finally, for each system, we show corner plots in Figure Set A10 of five astrophysically interesting parameters, including the primary and companion masses $M_{\rm pri}$ and $M_{\rm sec}$, semi-major axis a, eccentricity e and inclination i, and their covariances.

7.1. *HD 29021 b*

Figure Set A10 shows the fitted posterior distributions for the orbital elements of HD 29021 b. All are Gaussian apart from the inclination, which is bi-modal with equal likelihoods for prograde and retrograde orbits: either $33\overset{\circ}{.}7^{+6.8}_{-4.9}$ or $146\overset{\circ}{.}3^{+4.9}_{-6.8}$. Although the RV data only cover one and a half periods, the RV orbit of HD 29021 b is well-constrained. For HD 29021 b, we obtain a dynamical mass of $4.47^{+0.67}_{-0.65} M_{\rm Jup}$, an eccentricity of $0.453^{+0.014}_{-0.013}$, and a semi-major axis of $74.29^{+0.61}_{-0.62}$ AU. The $M \sin i$ inferred from our fit is $2.483^{+0.070}_{-0.068} M_{\rm Jup}$. We compare our orbital solution with the only orbital fit for this system published by Rey et al. (2017) where $M \sin i = 2.4 \pm 0.2 M_{\rm Jup}$, $e = 0.459 \pm 0.008$, $a = 2.28^{+0.07}_{-0.08}$, and $P = 3.732^{+0.013}_{-0.012}$ years; all of our parameters are consistent with this orbital solution.

7.2. *HD 81040 b*

HD 81040 b has the shortest period in our sample; the RV orbit is well-constrained by the joint HIRES and ELODIE RV data (see Figure Set A1). The posterior distributions of selected parameters for HD 81040 are displayed in Figure Set A10. Our orbital inclination indicates that it presents itself as an edge-on system with an orbital inclination of either $73°^{+12}_{-16}$ or $107°^{+16}_{-12}$. Our solution reveals that the true mass of HD 81040 b is $7.24^{+1.0}_{-0.37} M_{\rm Jup}$, slightly higher than these previous RV-only $M \sin i$ values. Out of the two $M \sin i$ values reported for this system, our inferred $M \sin i = 6.87 \pm 0.19\, M_{\rm Jup}$ agrees better with a value of $6.86 \pm 0.71\, M_{\rm Jup}$ from Sozzetti et al. (2006) than a value of 7.27 ± 0.98 from Stassun et al. (2017). The orbit of HD 81040 b is consistent with being edge-on: we find a 0.9% probability that the planet will transit. If it does transit, we predict transit times of 2021-11-11 and 2024-10-08, each with an unfortunately large uncertainty of about 25 days.

7.3. *HD 87883 b*

The posterior probability distributions of selected parameters and their covariances for HD 87883 b are shown in Figure Set A10. The posterior for the semi-major axis is bi-modal, peaking at 3.7 AU and 3.9 AU, respectively. Both the prograde and retrograde orbital inclinations are relatively face-on with values of $16\overset{\circ}{.}8^{+1.7}_{-1.4}$ and $163\overset{\circ}{.}1^{+1.4}_{-1.7}$. Figure Set A1 shows the HIRES and Hamilton RVs, and the corresponding best-fit Keplerian models and the residuals. Two families of orbits are possible; current RV data are insufficient to completely constrain the planet's semi-major axis and eccentricity.

HD 87883 was assessed by Fischer et al. (2009) prior to the 2007 publication of the HIRES/Keck RVs. Their eccentricity was poorly constrained ($e \geq 0.4$) due to the incomplete coverage of the orbital phase approaching periastron. Using the extra RV data, we find consistent orbital parameters with Fischer et al. (2009) and Stassun et al. (2017) except for $M \sin i$ where we find

a higher value. HD 87883's orbit is face-on and eccentric from our analysis. Our most likely orbit yields $M = 6.31^{+0.31}_{-0.32}\,M_{\rm Jup}$, a=$3.77^{+0.12}_{-0.094}$ AU, P=$8.23^{+0.32}_{-0.34}$ years, and $e = 0.720^{+0.038}_{-0.027}$. Still, further RV monitoring of target will be required to fully constrain its orbit.

7.4. *HD 98649 b*

The posterior distributions for HD 98649 b are depicted in Figure Set A10, and the fits to the RVs and astrometric accelerations are shown in Figure Set A1. Our solution shows that HD 98649 b is a highly eccentric and massive planet with an eccentricity of $0.852^{+0.033}_{-0.022}$ and a true planetary mass of $9.7^{+2.3}_{-1.9}\,M_{\rm Jup}$. There are two possible inclinations: either $136\overset{\circ}{.}3^{+8.1}_{-13}$ or $43\overset{\circ}{.}7^{+13}_{-8.1}$. The orbit of HD 98649 b was studied in Rickman et al. (2019) and Marmier et al. (2013). Both studies agree on a $M\sin i$ value of around $6.8 \pm 0.5\,M_{\rm Jup}$, and an eccentricity $e = 0.85 \pm 0.05$ but digress on the semi-major axis and the period of the system. We obtain a value of $a = 5.97^{+0.24}_{-0.21}$ AU, which agrees with a value of $a = 5.6 \pm 0.4$ AU found by Marmier et al. (2013), and marginally with the value of $6.57^{+0.31}_{-0.23}$ AU derived by Rickman et al. (2019).

7.5. *HD 106252 b*

The posterior probabilities for HD 106252 b are illustrated in Figure Set A10. The posterior probabilities follow nearly Gaussian distributions, except for the orbital inclination. The inclination is slightly bimodal, depending on whether the companion is in retrograde or prograde orbital motion. Figure Set A1 demonstrates the agreement between the calibrated *Hipparcos*-*Gaia* proper motions from the HGCA. As shown in Figure Set A1, the RV orbit of HD 106252 b is well-constrained thanks to full orbital phase coverage from 12 years of RV data. We obtain relatively tight constraints on the dynamical mass of the system, with $M = 10.0^{+0.78}_{-0.73}\,M_{\rm Jup}$, and an orbital inclination of $46\overset{\circ}{.}0^{+4.9}_{-4.1}$ (or $134\overset{\circ}{.}0^{-4.9}_{+4.1}$). Our derived $M\sin i$ of $7.20 \pm 0.13\,M_{\rm Jup}$ corroborates the dynamical analyses of Wittenmyer et al. (2009), Stassun et al. (2017) and Liu et al. (2014) within 5%. Other orbital parameters such as semi-major axis, period, and eccentricity are also in perfect agreement with results obtained by these authors.

7.6. *HD 106515 Ab*

The orbits of both HD 106515 Ab and HD 106515 B in the three-body system HD 106515 Ab are fully constrained (see Figure Set A1). The induced astrometric acceleration by HD 106515 Ab on HD 106515 A is the most significant in our list. The posterior distributions for HD 106515 Ab and HD 106515 B are shown in Figure Set A10. Our 3-body fit reveals a brown dwarf companion to HD 106515 A with a precise dynamical mass of $18.9^{+1.5}_{-1.4}\,M_{\rm Jup}$ on a ≈10-year period. Our $M\sin i$ value of $9.25 \pm 0.25\,M_{\rm Jup}$ agrees with the $9.08 \pm 0.14\,M_{\rm Jup}$ from Saffe et al. (2019)'s analysis within 2%. All other fitted parameters are also in agreement with Saffe et al. (2019) and Marmier et al. (2013).

Our three-body fit yields a semi-major axis of 335^{+96}_{-42} AU for the HD 106515 A/B binary. This is consistent with a 201 AU projected separation given in *Gaia* EDR3 (see Table 3) and a 329 AU semi-major axis value provided in Marmier et al. (2013) based on the positions given by Gould & Chaname (2004). Rica et al. (2017) also found a semi-major axis of 345 AU and an eccentricity of about 0.42 that agrees with ours.

7.7. *HD 171238 b*

Our best-fit orbit for HD 171238 b reveals a dynamical mass of $8.8^{+3.6}_{-1.3}\,M_{\rm Jup}$, an $M\sin i = 2.599^{+0.090}_{-0.088}\,M_{\rm Jup}$, a semi-major axis of $a = 2.519^{+0.032}_{-0.033}$ AU and an eccentricity $e = 0.358^{+0.028}_{-0.026}$, all with tight 1σ errors. The MCMC posterior (Figure Set A10) for the mass of HD 171238 b shows a secondary peak around $15\,M_{\rm Jup}$. The RV orbit presented in Figure Set A1 is constrained by three RV instruments. The inclination ($17\overset{\circ}{.}1^{+3.1}_{-5.0}$ or $162\overset{\circ}{.}9^{+5.0}_{-3.1}$) from our solution indicates a relatively face-on orbit for HD 171238 b. The $M\sin i$, eccentricity and semi-major axis are more consistent with the orbit analysis of Ségransan et al. (2010) ($M\sin i = 2.60 \pm 0.15 M_{\rm Jup}$, $a = 2.54 \pm 0.06$ AU and $e = 0.400^{+0.061}_{-0.065}$) than that of Ment et al. (2018). HD 171238 b's mass is bimodal, possibly either $\approx 9 M_{\rm Jup}$ or $\approx 15 M_{\rm Jup}$. Future *Gaia* data releases will confirm the planet's orbit and mass.

7.8. *HD 196067 b*

HD 196067 b is in a 3-body system with HD 196067 and HD 196068, HD 196067 being the host star and HD 196068 being the stellar companion to HD 196067. The wide orbit stellar companion HD 196068 does accelerate HD 196067, though the >1000 AU separation results in a minimal contribution to the astrometric acceleration from HD 196068. Our MCMC posteriors from the 3-body fit with `orvara` are shown in Figure Set A10 for the inner and outer companions, respectively.

The RV orbit of HD 196067 b (see Figure Set A1) is not perfectly constrained. CORALIE-98 data did not sufficiently sample the sharp turnaround region near periastron. This lack of data results in a bimodal distribution for the eccentricity in the MCMC posteriors, one near $e = 0.6$ and the other near $e = 0.85$ (see Figure Set A10). For HD 196067 b, our 3-body solution favors a dynamical mass of $12.5^{+2.5}_{-1.8}\,M_{\rm Jup}$, a semi-major axis of

$5.10^{+0.22}_{-0.17}$, and an orbital period of $9.88^{+0.63}_{-0.43}$ years. The orbital period is consistent with the minimum period of 9.5 years found by Marmier et al. (2013) who have studied the system using the same data as us. They also found an eccentricity of $e = 0.66^{+0.18}_{-0.09}$, which is more consistent with the lower peak (e≈ 0.60) than the higher one in our bi-modal eccentricity posteriors. The inclination distribution is again, bi-modal: either $41°2^{+28}_{-9.1}$ or $138°8^{+9.1}_{-28}$. We find that its true mass was underestimated by RV-only works. Our estimate of its true dynamical mass of $12.8^{+2.6}_{-1.8}\,M_{\rm Jup}$ is nearly twice as much as the minimum mass found by Marmier et al. (2013). HD 196067 b is interesting as it lies extremely close to the deuterium burning limit (Spiegel et al. 2011) that divides planets and brown dwarfs. We expect that further RV data near the periastron passage of the companion will enable us to finalize its full orbit and confirm the dynamical nature of this companion.

The posterior distributions for HD 196068 are shown in Figure Set A10. The inclination of the stellar companion HD 196068, instead of being bi-modal, has a single value of $10.^{\circ}6^{+6.1}_{-5.2}$, suggesting a nearly face-on orbit. This is because the single relative astrometric measurement from *Gaia* at epoch 2016.0 described in Section 5 successfully differentiated prograde from retrograde orbits of HD 196068. Our 3-body solution leads to a projected binary semi-major axis of 1631^{+208}_{-213} AU, significantly higher than a value of 932 AU in (Marmier et al. 2013). This can be explained by the stellar companion being near apastron in an eccentric orbit where $e = 0.731^{+0.026}_{-0.031}$.

7.9. *HD 221420 b*

The posterior distributions for selected parameters for HD 221420 b from the joint orbit fit are illustrated in Figure Set A10. The RV orbits and astrometric proper motions are displayed in Figure Set A1. The best fit curves agree with both the RV data and proper motions from the HGCA.

The orbital solution for HD 221420 b was first derived by Kane et al. (2019) using only the AAT RVs. This orbital solution presents a period of $61.55^{+11.50}_{-11.23}$ years, an eccentricity of $0.42^{+0.05}_{-0.07}$, a semi-major axis of $18.5^{+2.3}_{-2.3}$ AU, and a minimum mass of $9.7^{+1.1}_{-1.0}M_{\rm Jup}$. This minimum mass is 36.5% discrepant with ours. This companion has recently been revisited by Venner et al. (2021) who use AAT and HARPS RVs, and Hipparcos-Gaia (DR2) astrometry to constrain the precise dynamical mass. They find an orbital inclination of $164.^{\circ}0^{+1.9}_{-2.6}$, a precise dynamical mass of $22.9 \pm 2.2\,M_{\rm Jup}$, a semi-major axis of $10.15^{+0.59}_{-0.38}$ AU, and a period of $27.62^{+2.45}_{-1.54}$ years. Using the AAT and HARPS RVs, and absolute astrometry from *Hipparcos* and *Gaia* EDR3, we obtain a companion mass of $20.6^{+2.0}_{-1.6}M_{\rm Jup}$, an eccentricity of $0.162^{+0.035}_{-0.030}$, a semi-major axis of $9.99^{+0.74}_{-0.70}\,AU$, and a period of $27.7^{+3.0}_{-2.5}$. Our EDR3 solution agrees well with that of Venner et al. (2021), with one distinction being our inclination is again bimodal with equal maximum likelihood: i = $178°5^{+2.9}_{-2.8}$ or $162.^{\circ}2^{+2.8}_{-2.9}$. We validate the findings by Venner et al. (2021) that the companion is near the $25M_{\rm Jup}$ upper limit for core accretion and disk instability to be considered plausible formation channels. Venner et al. (2021) also identify a M-dwarf stellar companion HD 221420 B that may be bound to HD 221420 A, but at a separation of more than 20,000 AU, it contributes negligibly to HD 221420's acceleration. HD 221420 b has the longest period and highest companion mass among the RV companions we sample. As a result, it is also the most accessible of our substellar companions for future direct imaging.

Direct imaging can probe the outer architecture of a system (Chauvin et al. 2005; Lafrenière et al. 2008; Ireland et al. 2010; Rameau et al. 2013; Lagrange 2014; Bowler 2016). However, only about a dozen wide-orbit giant planets have been discovered at separations of ∼10-150 AU of their host stars (e.g. Chauvin et al. 2018; Marois et al. 2008). These surveys have mostly been blind. HD 221420b represents a rare case of a substellar companion whose mass and position we can determine before imaging.

We use our orbital fit to predict the position of HD 221420 b at future epochs. In Fig. 3, we show the predicted locations of HD 221420 b at epochs 2022.0 and 2023.0, 2024.0, and 2025.0. Despite the fact that HD 221420 b has never been imaged, our 68% confidence interval places it within a box of about 100 × 200 mas, almost sufficient to locate a fiber for the GRAVITY interferometer (Gravity Collaboration et al. 2017). For the next couple of years the brown dwarf will be offset about $0.''4$ west of its host star in a slow orbit. Unfortunately, we lack the data to establish whether this orbit is clockwise or counter-clockwise on the sky.

HD 221420 b is an unusually promising accelerating system for high-contrast imaging follow-up. It consists of a relatively low-mass brown dwarf orbiting a bright ($V = 5.8$) and nearby ($d = 31.2$ pc) host star. Depending on the system age (Section 2.4), the ATMO2020 evolutionary models (Phillips et al. 2020) predict an effective temperature of 400-600 K for HD 221420 b. These low temperatures correspond to a late-T or early-Y spectral type. The H-band contrast predicted from ATMO2020 ranges from 16 to 20 magnitudes depending on the brown dwarf's mass and the system age, while the predicted L' contrast ranges from 13 to 15

magnitudes. These exceed the typical performance of SPHERE (Beuzit et al. 2008) but may be achievable with long integrations and, as Figure 3 shows, with the knowledge of where to look.

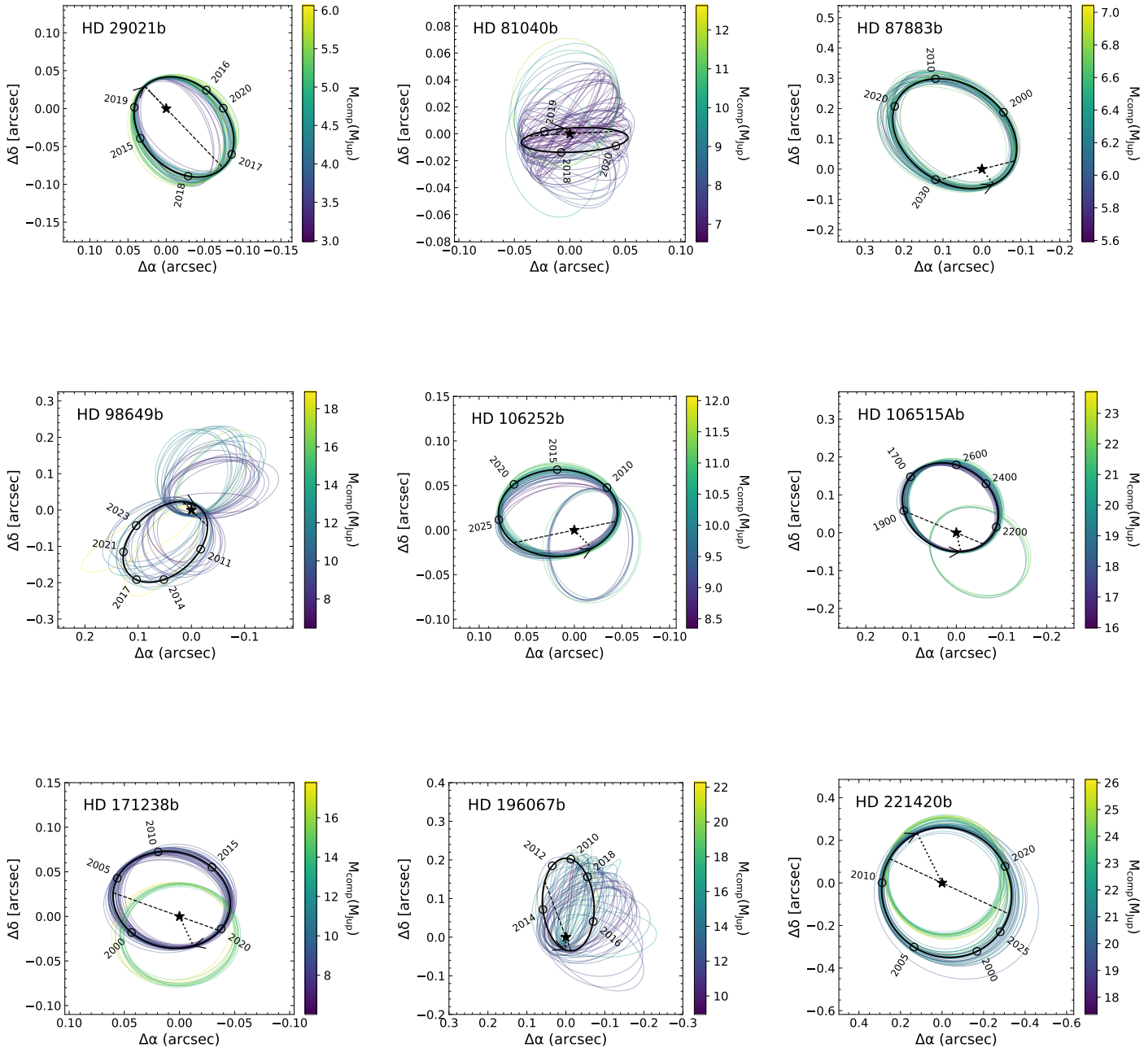

Figure 2. Relative astrometric orbits of the nine companions studied in this paper. The thick black lines indicate the best-fit orbit and the colorful thin lines are 50 orbits drawn randomly from corresponding posterior distribution, color-coded by the mass of the secondary companion from purple (low mass) to yellow (high mass). The dashed lines are the line of nodes connecting the host star to the companion's periastron passage. The arrows on the best-fit orbit indicate the direction of motion of the companion revolving around the host star. The hollow circled points label selected epochs along the orbit.

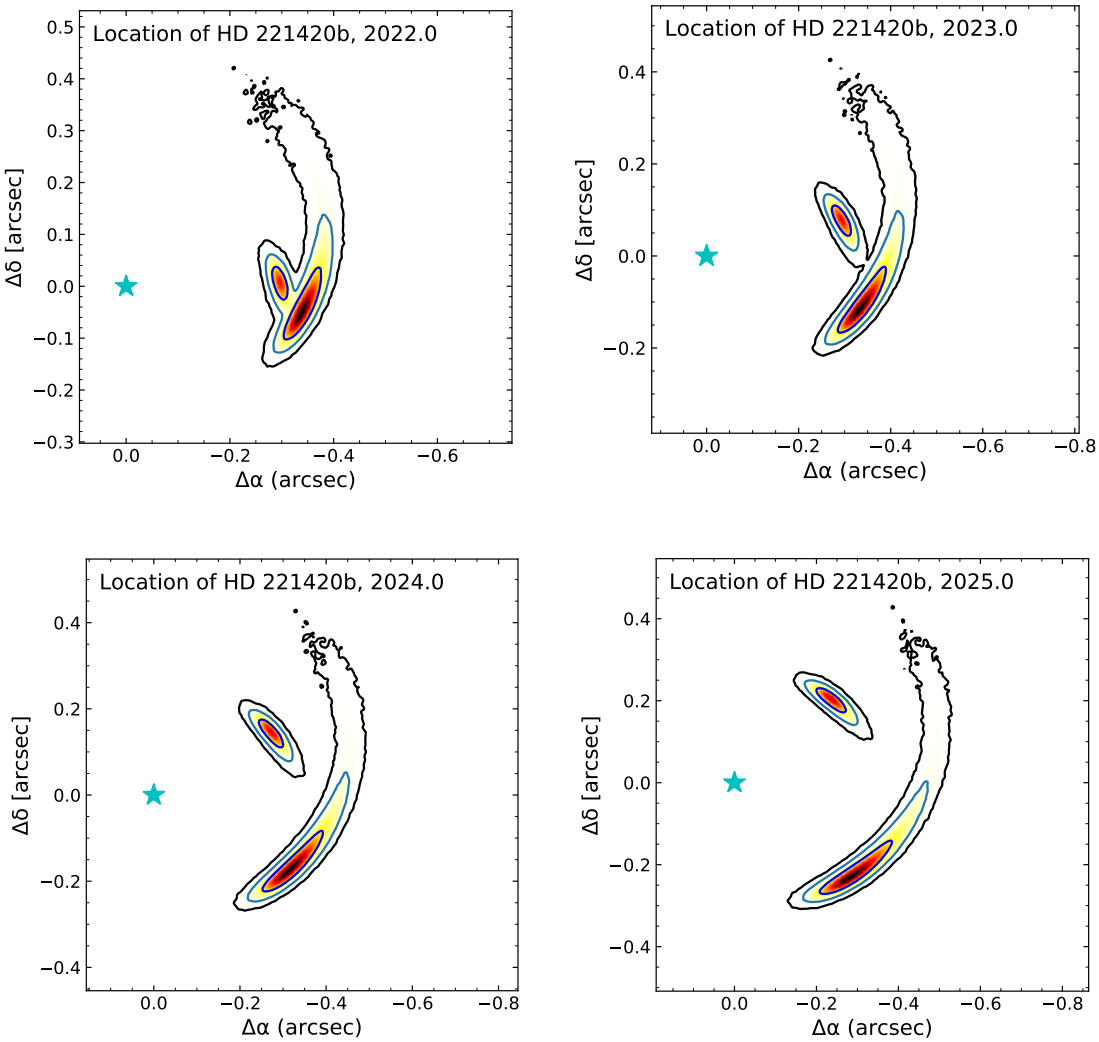

Figure 3. Predicted positions of HD 221420 b in epoch 2022, 2023, 2024, and 2025. The light blue stars denote the host star HD 221420. The contours indicate the predicted relative coordinates of the brown dwarf companion HD 221420 b with respect to the location of the host star. The contour lines enclose the 1σ, 2σ and 3σ probabilities with descending normalized likelihood from inner to outer contours (black to red to light yellow). Two possible sets of contours correspond to prograde or retrograde orbits. If the companion can be resolved via high-contrast imaging, it will eventually tell the two orbital motions apart.

8. DISCUSSION AND CONCLUSION

In this paper, we have refined orbital solutions for nine single RV companions orbiting G and K-type stars using the orbit-fitting package `orvara`. For every target, we have obtained 1σ error bars on the dynamical masses, and we find bi-modal orbital inclinations. Apart from HD 221420 b recently assessed by Venner et al. (2021), no past dynamical mass measurements were available for the RV companions we study. This motivates us to compare our $M \sin i$ with previous RV-only $M \sin i$ values. Our $M \sin i$ values agree with the literature reports within 1σ. Fig. 4 compares the minimum mass and true mass of each companion from our orbital fits. The RV-only minimum companion masses were underestimated due to uncertain inclinations by at least $\approx$ 5 percent and at most $\approx$ 250 percent. The mass increase is greater for more face-on orbits such as that of HD 87883 b, HD 171238 b, and HD 221420 b, and less so for edge-on orbits like that of HD 81040b.

Several of our companions have periods comparable to the 33-month *Gaia* EDR3 baseline: HD 29021 b ($3.737^{+0.018}_{-0.018}$ years), HD 81040 b ($2.7452^{+0.011}_{-0.0093}$ years), HD 106252 b ($4.202^{+0.011}_{-0.010}$ years), and HD 171238 b ($4.148^{+0.045}_{-0.046}$ years), with the shortest being HD 81040 b. The other five – HD 87883 b, HD 98649 b, HD 106515 Ab, HD 196067 b, HD 221420 b – have long periods ≥ 8 years. The Renormalised Unit Weight Error (RUWE) of the short-period planet HD 81040 b (=1.598) is slightly higher than the usual good astrometry solution *Gaia* recommends of <1.4 (Gaia Collaboration et al. 2018). Since there is no evidence of its binarity in the literature, the anomaly in RUWE may be attributed to the perturbation effects from HD 81040 b, its $7.24^{+1.0}_{-0.37}\,M_{\rm Jup}$ planetary companion. Furthermore, given that its orbital period is comparable to the 33-month baseline of *Gaia* EDR3, it is challenging to constrain its astrometric orbital motion without the *Gaia* intermediate astrometric data. In their absence, all epoch astrometry data are forward-modeled by `htof`. Brandt et al. (2021a) has tested the fidelity of `htof` on data integration against the `REBOUND` code for a 3-body `orvara` fit to the short period planet β Pictoris c, and found that `htof` and `orvara` recover the `REBOUND` fit. Future *Gaia* data releases will include non-single star fits and epoch astrometry, enabling precise orbital fits to these shorter-period systems.

Interestingly, once masses and inclinations are separately constrained, the true dynamical masses of some of these companions are revealed to be much higher than the literature RV-only minimum masses. HD 196067 b, with a true mass of $12.5^{+2.5}_{-1.8}\,M_{\rm Jup}$, lies on the transition between giant planets and brown dwarfs according to the $13\,M_{\rm Jup}$ upper mass limit for the ignition of deuterium Boss (2008); Spiegel et al. (2011). HD 106515 Ab and HD 221420 b are rare long period and low-mass brown dwarfs ($\approx 20\,M_{\rm Jup}$) according to this deuterium-burning mass limit. HD 87883 b, HD 171238 b, and HD 221420 b have almost face-on orbits and, as a result, high masses. This places them in the population suggested by Schlaufman (2018) to be uncorrelated with host star metallicity, though spectroscopic measurements find each of these stars to be of super-Solar metallicity. Our finding of several companions with relatively face-on inclinations may be a selection effect: we have fit stars with signficant astrometric accelerations in the HGCA. Many of our inclinations have bimodal posteriors; these will be resolved with future *Gaia* data releases.

Eccentricities of planets provide insights into their dynamical history and formation mechanisms. Bowler et al. (2020) conducted a population-level study of the eccentricity distributions of directly imaged companions. They found that the eccentricity distribution peaks around $e = 0.23$ for single long-period giant planets, around $e = 0.5$ for brown dwarf on closer orbits (5-30 AU), and around $e = 0.6$ for low-mass companions within 10 AU.

Three of our wide orbit companions—HD 87883 b, HD 98649 b, and HD 196067 b—have high eccentricities >0.7. HD 81040 b and HD 106515 Ab also have moderately high eccentricities of between 0.5 and 0.6. HD 221420 b has a surprisingly low eccentricity of $0.162^{+0.035}_{-0.030}$, much lower than the mean eccentricity of $e = 0.5$ found by Bowler et al. (2020) for short-period brown dwarfs. HD 98649 b, with $e = 0.822^{+0.030}_{-0.024}$ is the most eccentric planet known with a period longer than 600 days and one of the more eccentric planetary orbits ever discovered.

HD 106515 Ab and HD 196067 b have outer stellar companions, raising the possibility that Kozai-Lidov (Kozai 1962; Lidov 1962) oscillations brought them onto highly eccentric orbits (Marmier et al. 2013). For HD 106515 Ab and HD 196067 b, the relative inclination angles between the orbital planes of the planet and the stellar companion are $10\overset{\circ}{.}4^{+8.2}_{-8.6}$ and $30\overset{\circ}{.}6^{+28.7}_{-10.5}$, respectively. The Lidov–Kozai interactions Kozai (1962); Lidov (1962) require a relative inclination angle of 39° in order to be invoked. This does not apply to HD 106515 Ab, but does apply to HD 196067 b whose relative inclination is subject to large uncertainties. The high orbital eccentricities of HD 87883 b and HD 98649 b may also be explained by the Kozi mechanism, but there's a lack of evidence of the existence of a third body in their systems. Precise *Hipparcos* and *Gaia* astrome-

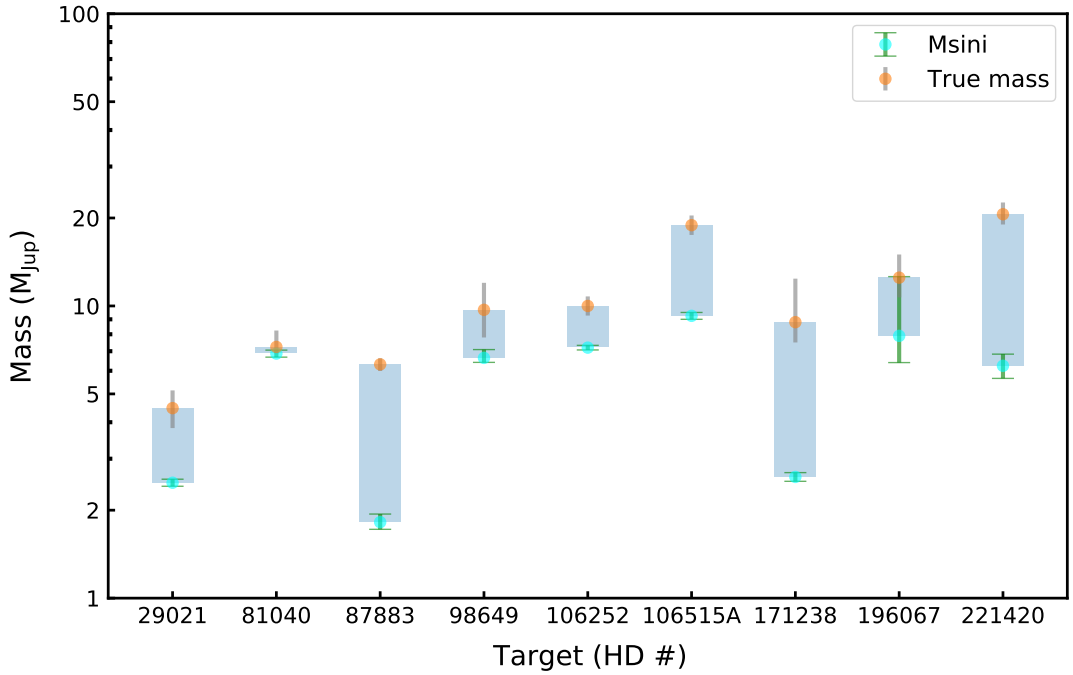

Figure 4. A summary of the differences in the final mass and Msini estimations for the nine RV companions studied in this work. The values for each companion are listed in Table 5. The orange points and grey error bars are the true dynamical masses derived by this work, and the cyan dots plus green error bars are the Msini values inferred from the orbital parameters in this work. The blue regions highlight how much the true dynamical masses can be underestimated by RV-only fits as a consequence of uncertain inclinations.

try over a 25-year baseline limits the parameter space in which additional, outer companions could be hiding.

HD 29021, HD 81040, and HD 106252 are rare examples of stars with giant planetary companions but with subsolar metallicity. This may support the finding by Adibekyan et al. (2013) that metal-poor stars host planets with longer periods than metal-rich stars. HD 81040 and HD 106252 seem to fall in the high-mass category suggested by Schlaufman (2018) to be uncorrelated with stellar metallicity. Our dynamical masses and orbits, including our substantial corrections to $M \sin i$ for several of our planets, will enable stronger comparisons between the masses of planets around metal-poor and metal-rich stars.

From our RV fits, four of the targets HD 87883 b, HD 171238 b, HD 98649 b and HD 196067 b need at least one more period of RV monitoring in order to completely constrain their orbital solutions. Our companions have typical separations of $\lesssim 0.2''$ and distances within 50 pc. The high contrasts needed to image these planets are on the order of a few 10^{-7} for HD 221420 b in the thermal near-infrared, and slightly worse for HD 106515 Ab. The remainder would have contrasts of $\sim 10^{-9}$ in reflected light depending on orbital phase and albedo. The current generation of high contrast imagers like SPHERE for VLT (Beuzit et al. 2008) and GPI for Gemini (Chilcote et al. 2018) may marginally resolve HD 221420 b. Most of our stars are old and their companions are very cold, so the companions are light-reflecting planets/low-mass brown dwarfs with little thermal emission. These companions will provide comparisons to thermal spectra of outer Solar system planets and very old field brown dwarfs. The systems we study are not the most favorable for the Coronagraph Instrument (CGI) on the Nancy Grace Roman Space Telescope (Kasdin et al. 2020): their $\sim 0.''2$ angular separations are too close. However, HD 106515 Ab and HD 221420 b are excellent targets for the Giant Magellan Telescope (GMT), the European Extremely Large Telescope (ESO ELT) , and the Thirty Meter Telescope (TMT).

Absolute astrometry can break the mass-inclination degeneracy inherent in RV work, and can enable the prediction of a planet's location on the sky. We have derived precise dynamical masses of nine planets in this work. Many still have an uncertain orientation on the sky, with existing astrometry unable to distinguish prograde from retrograde orbits. This will change conclusively with future *Gaia* data releases, as *Gaia* achieves the temporal coverage needed to map out orbits on its own. The synergy between RV and absolute astrometry

will then enable precise mass and orbit measurements for all of the nearby giant exoplanets.

APPENDIX

Figures A1-A20 show the full results from the `orvara` orbital fits to the 11 companions (nine planets and brown dwarfs, plus two stellar companions) in nine systems. Figures A1-A9 show the radial velocity measurements and fitted orbits in the left panels, and the absolute astrometry in the right panels. Figures A10-A20 show corner plots of the astrophysically interesting parameters: masses, semimajor axis, and eccentricity, along with inclination.

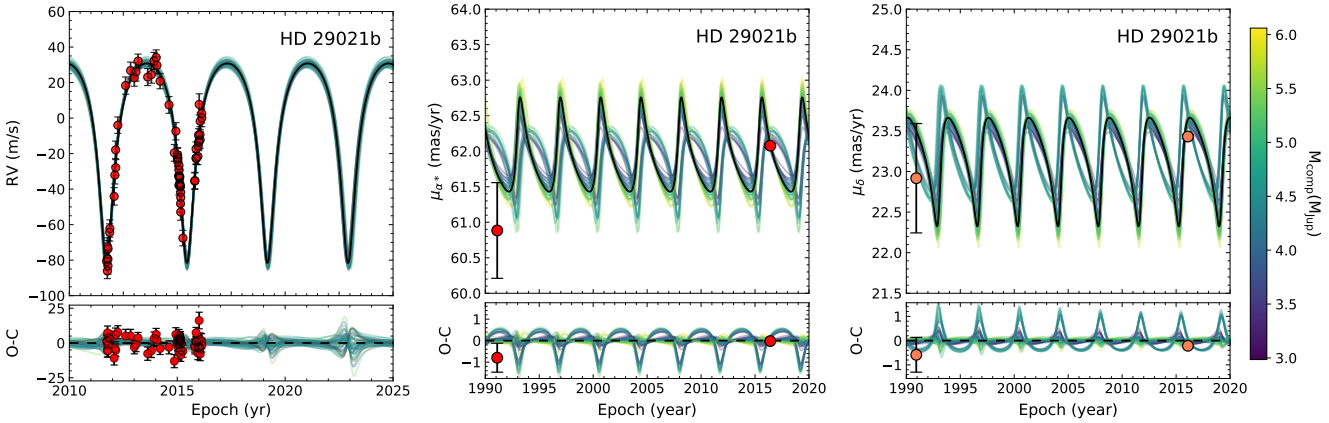

Figure A1. Left panel: Radial Velocity orbit for HD 29021 b. The RV data are from the OHP 1.93m SOPHIE spectrograph. Middle and right panels: astrometric acceleration in right ascension and declination. The red and orange points are proper motion measurements from *Hipparcos* near epoch 1991 and *Gaia* near epoch 2016. The thick black lines indicate the best-fit orbits in the MCMC chain while the colored lines are solutions randomly drawn from the chain, color-coded by the dynamical mass of the companion.

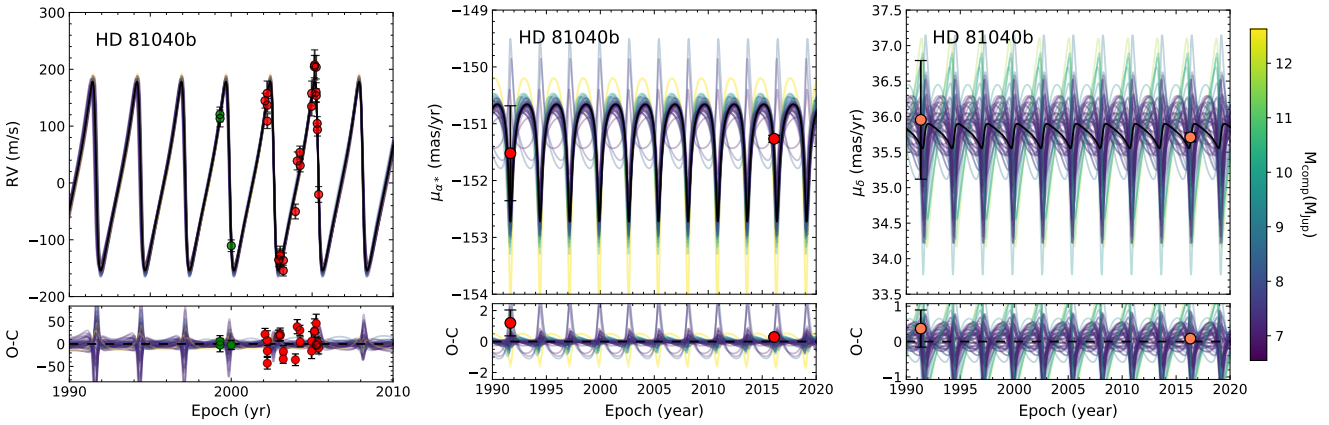

Figure A2. HD 81040 b. Same as Fig. A1. Data for RVs come from HIRES/Keck (green) and ELODIE (red).

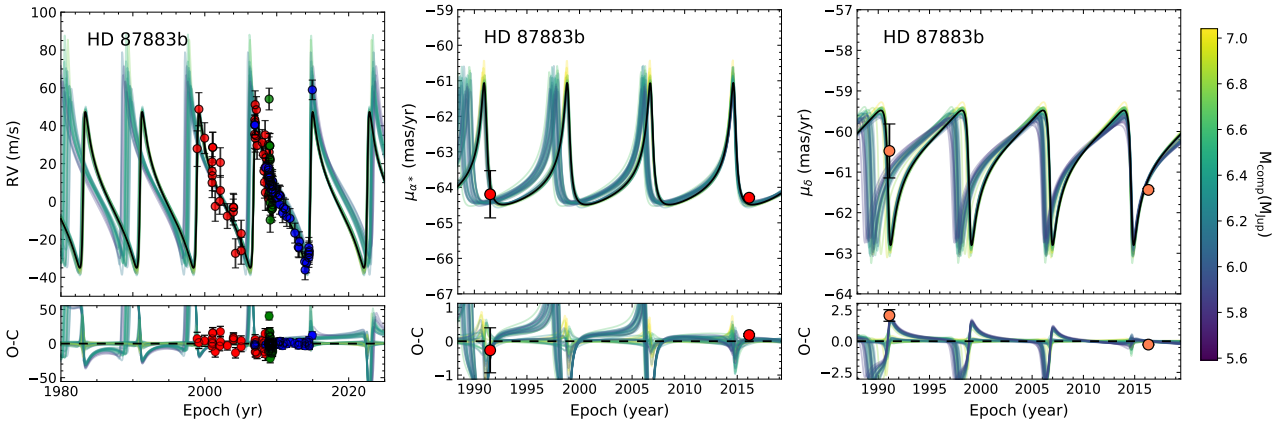

Figure A3. HD 87883 b. Same as Fig. A1. Red and blue points with error bars are RVs from Hamilton/Lick published in 2009 and 2017, respectively, and the green points are velocities from HIRES/Keck.

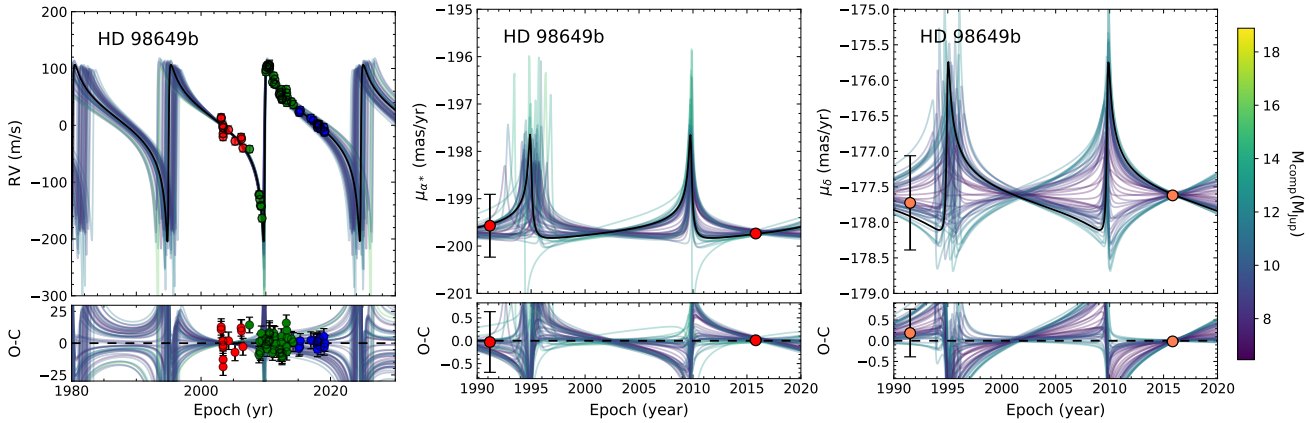

Figure A4. HD 98649 b. Same as Fig. A1. The red and green data points in the left panel are RVs from CORALIE-98 and CORALIE-07, respectively.

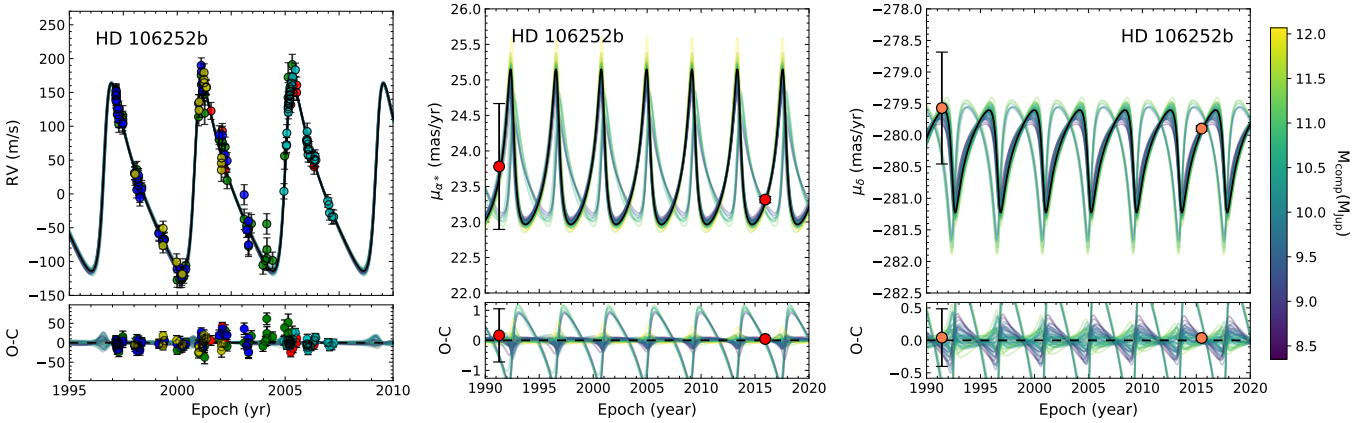

Figure A5. HD 106252 b. Same as Fig. A1. The solid circles and error bars in the left most panel represent RVs from ELODIE (blue), Hamilton/Keck (yellow and green), CDES-TS2 (red), and HRS/HET (cyan).

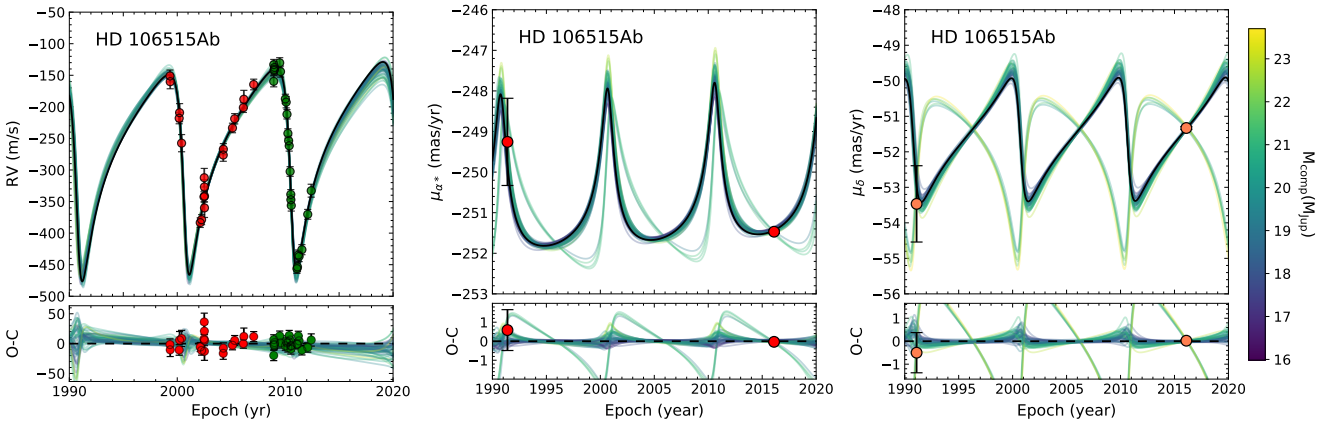

Figure A6. HD 106515 Ab. Same as Fig. A1. Red and green RV data show CORALIE-98 and CORALIE-07 measurements, respectively.

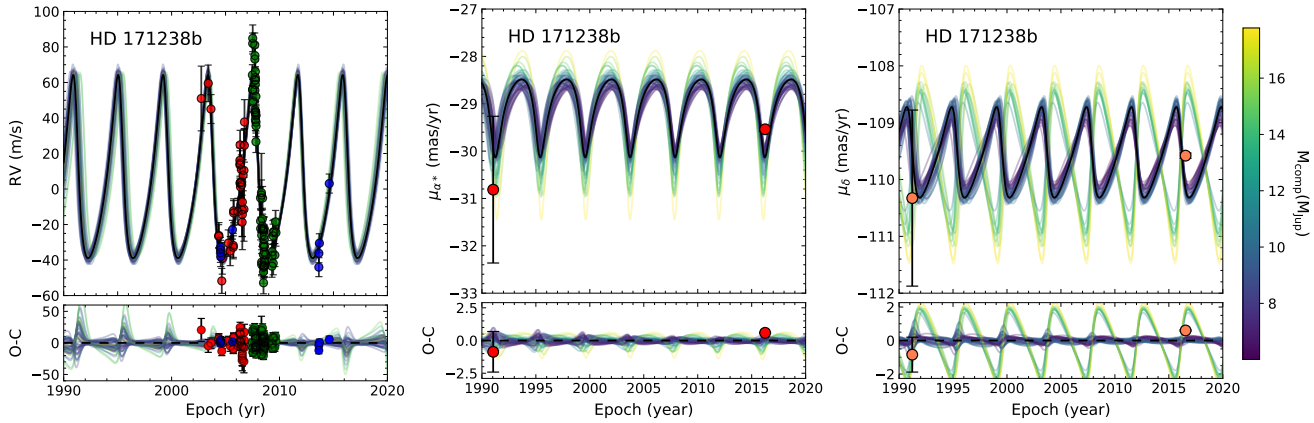

Figure A7. HD 171238 b. Same as Fig. A1. In the left panel, the RVs from CORALIE-98 are in red, the velocities from CORALIE-07 are in green, and the blue data points represent velocities from HIRES/Keck published in 2017.

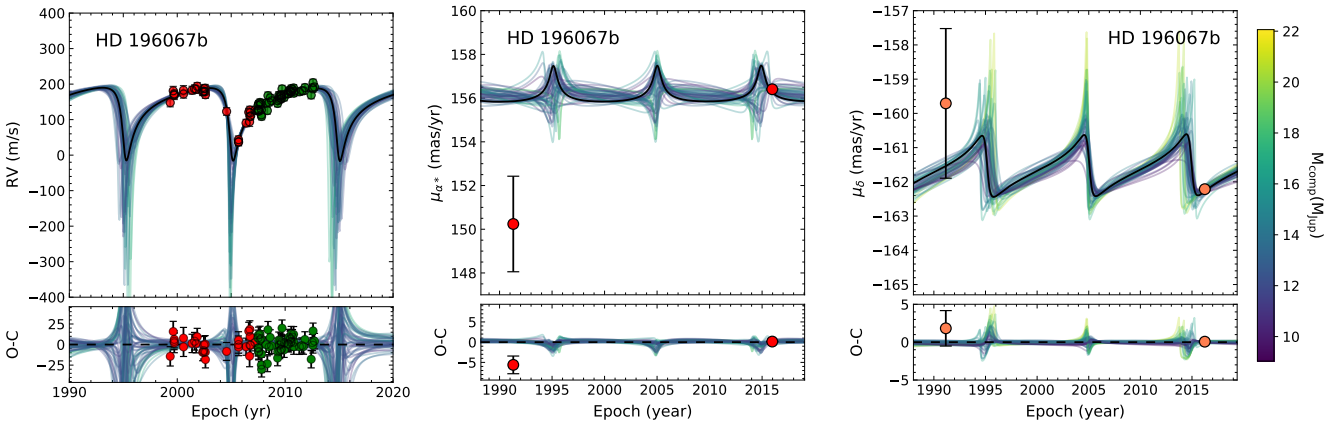

Figure A8. HD 196067 b. Same as Fig. A1. The RV measurements are from CORALIE-98 (red) and CORALIE-07 (green).

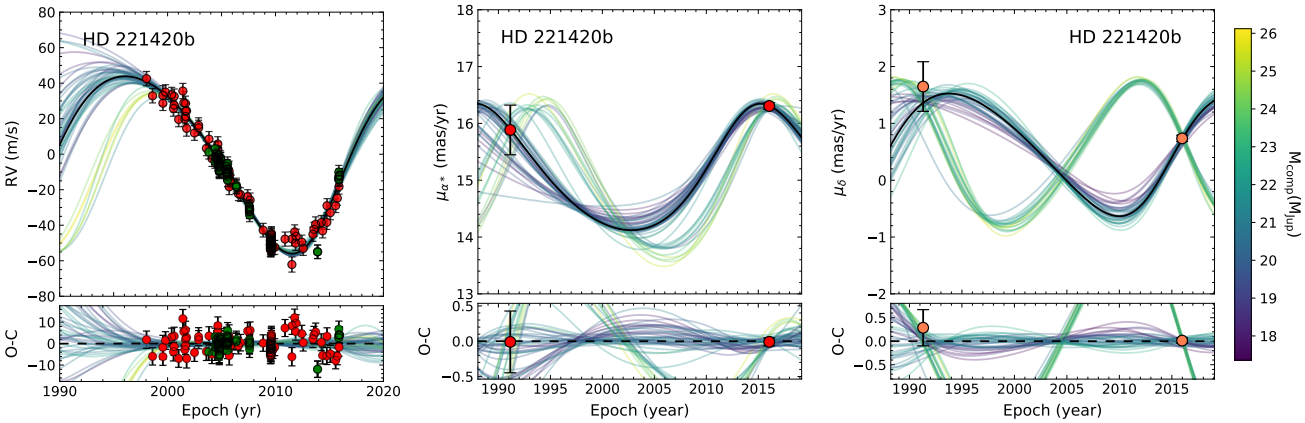

Figure A9. HD 221420 b. Same as Fig. A1. In the left panel, the red data points show RVs from AAT, and the HARPS RVs are showcased by green data points.

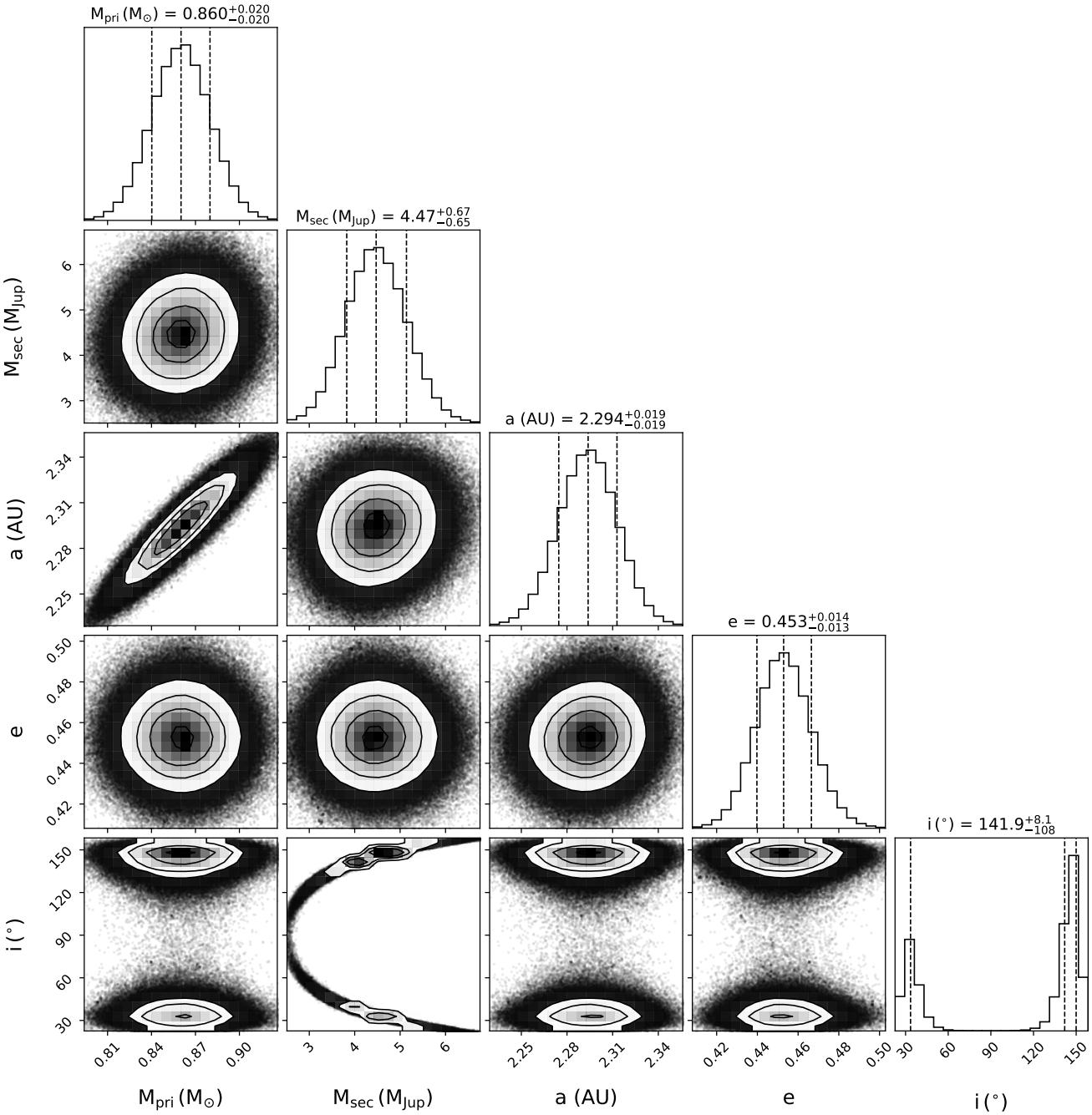

Figure A10. Joint posterior distributions for selected orbital parameters of HD 29021 b. These are the host star's mass (M_{pri}), the companion mass (M_{sec}), the semi-major axis a, the orbital eccentricity e, and the orbital inclination i. The values and histogram distributions of the posteriors of selected parameters are shown, along with 1 σ uncertainties.

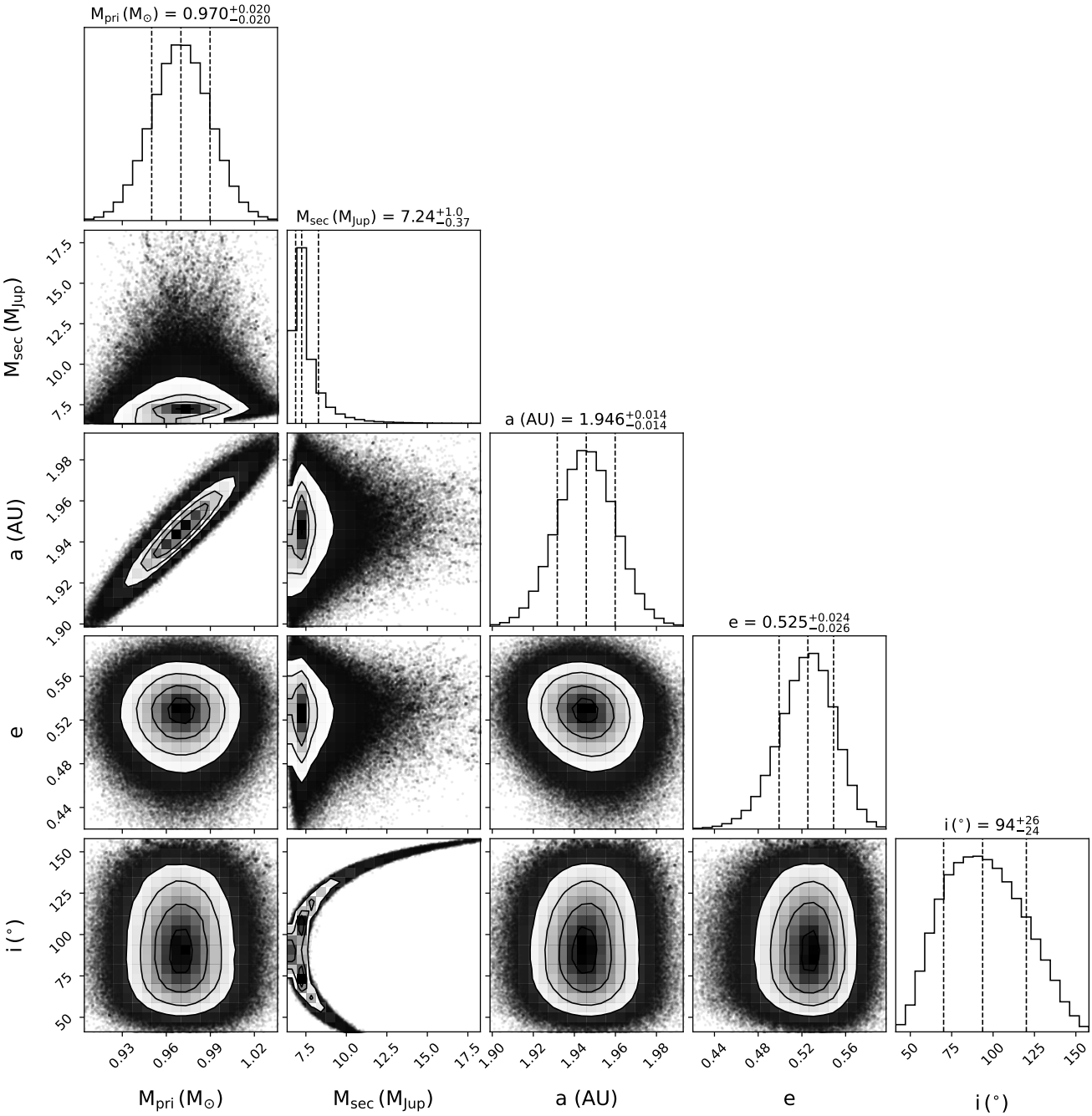

Figure A11. HD 81040 b. Same as Fig. A10.

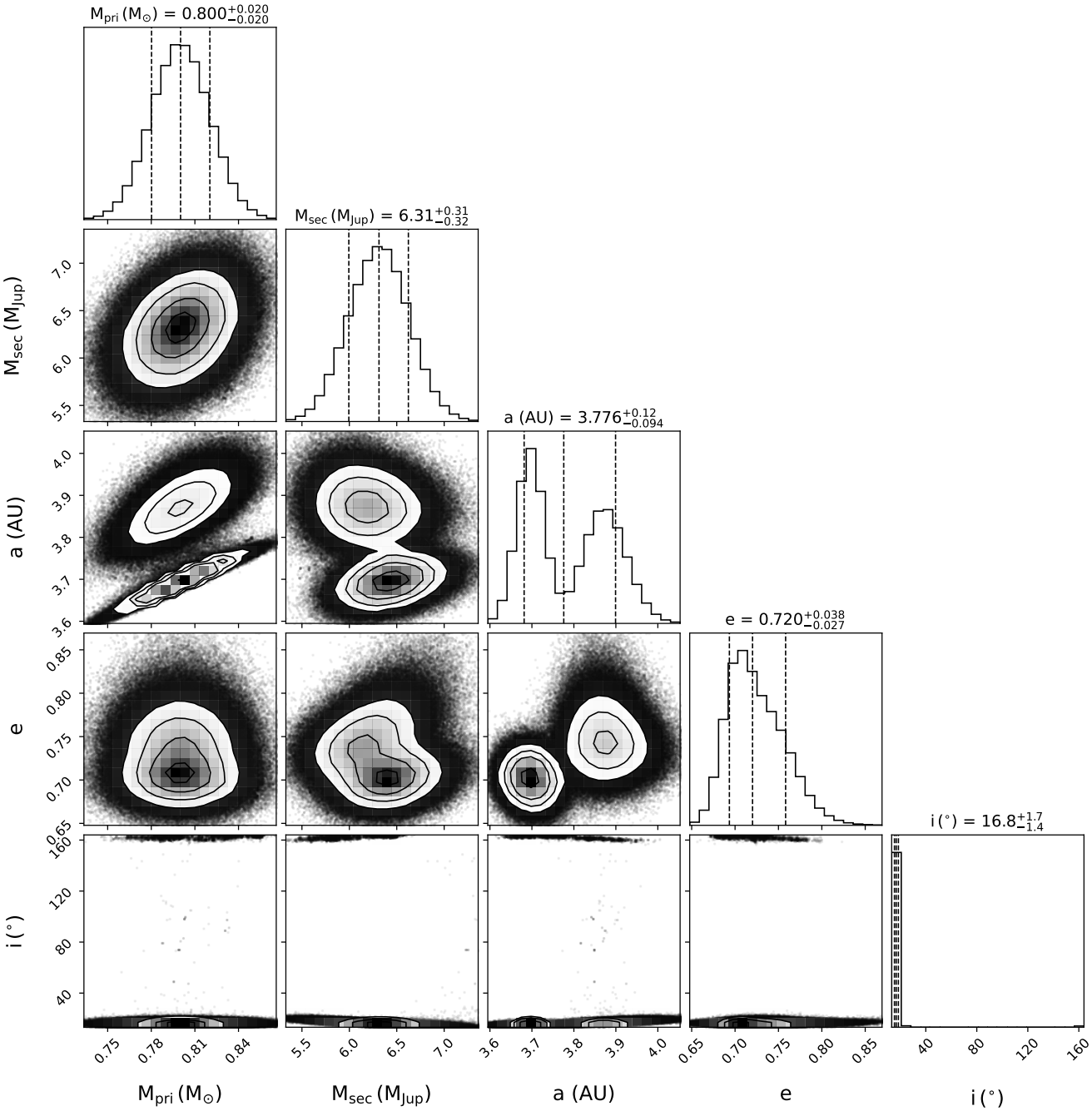

Figure A12. HD 87883 b. Same as Fig. A10.

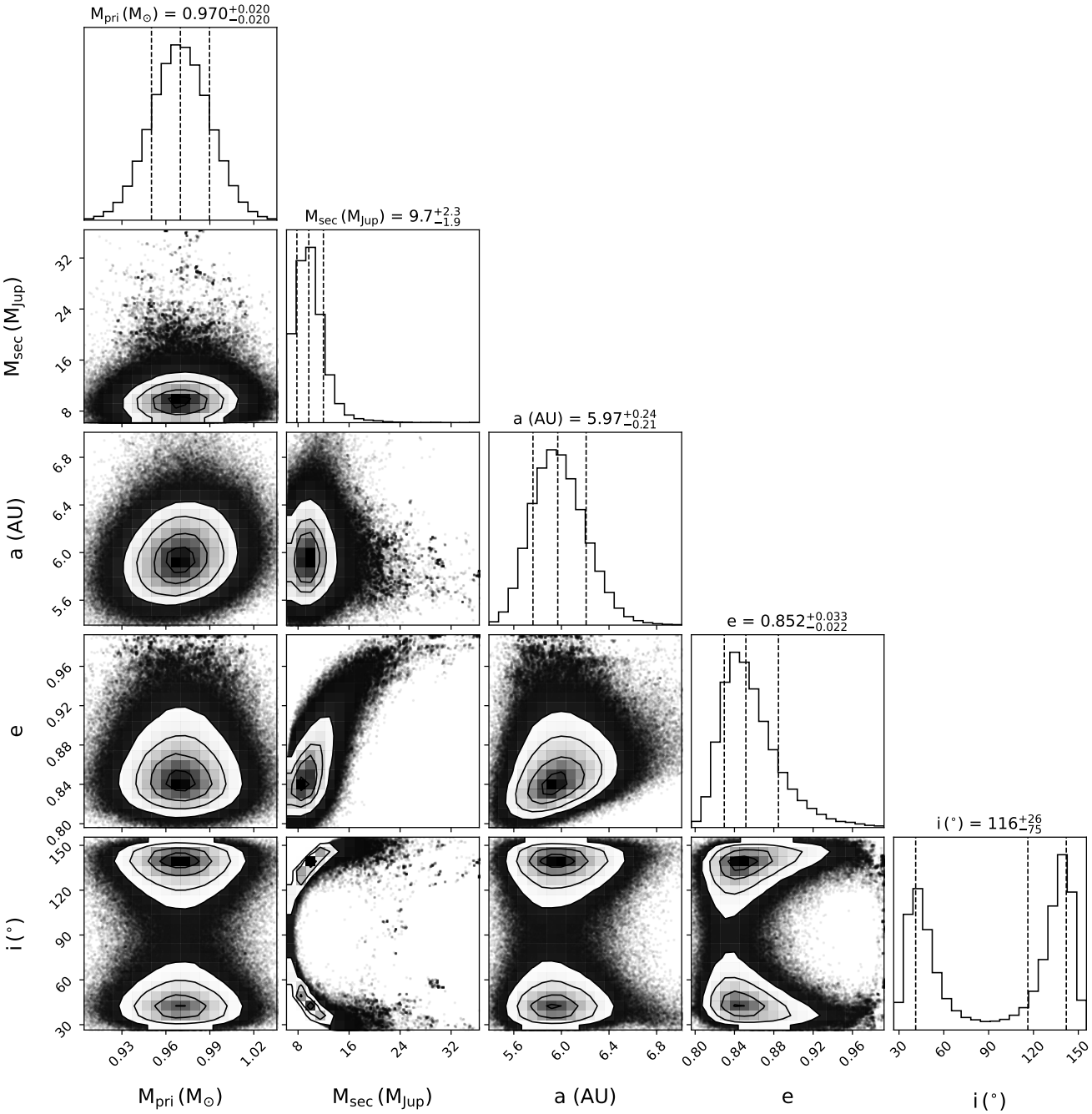

Figure A13. HD 98649 b. Same as Fig. A10.

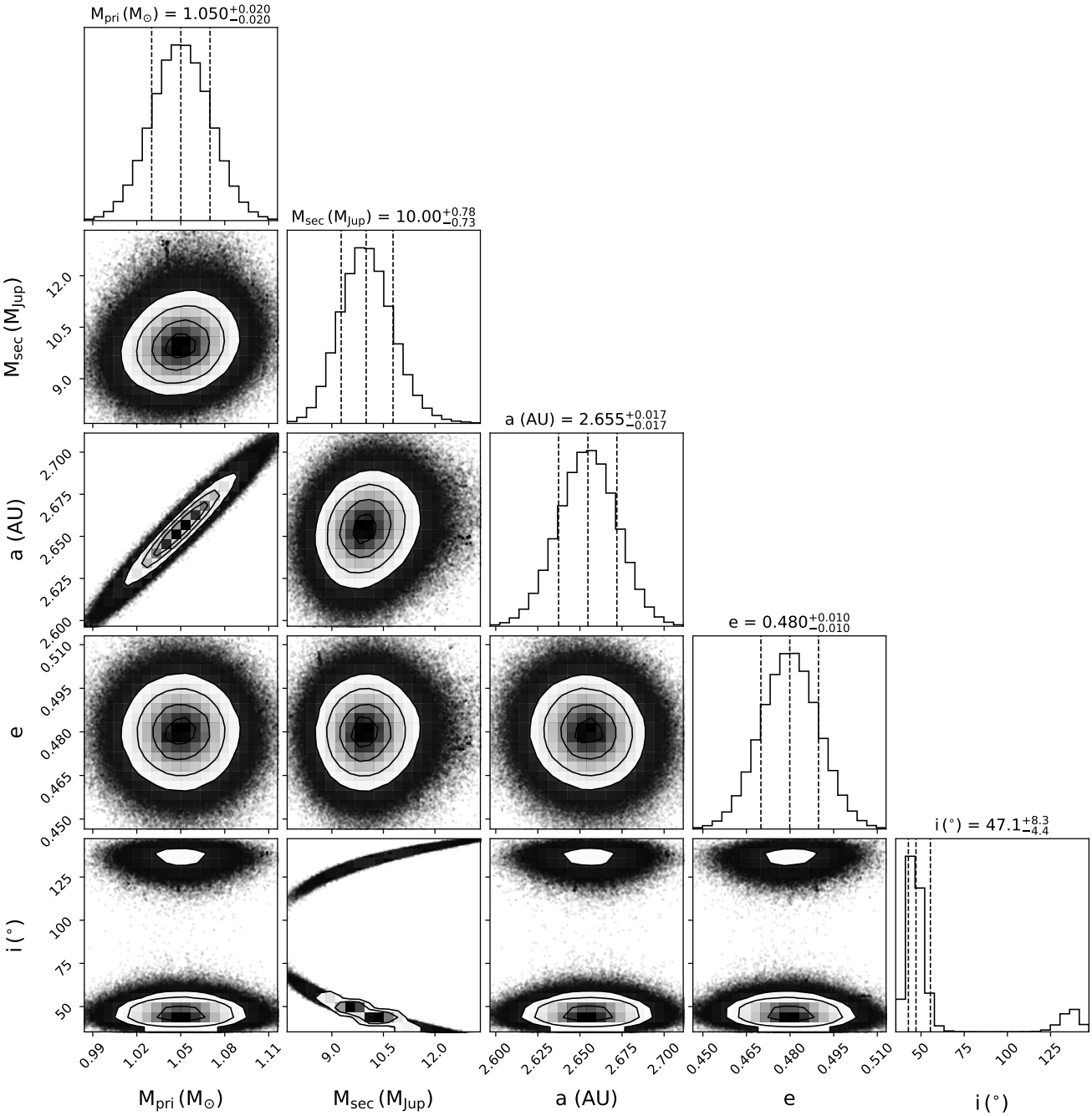

Figure A14. HD 106252 b. Same as Fig. A10.

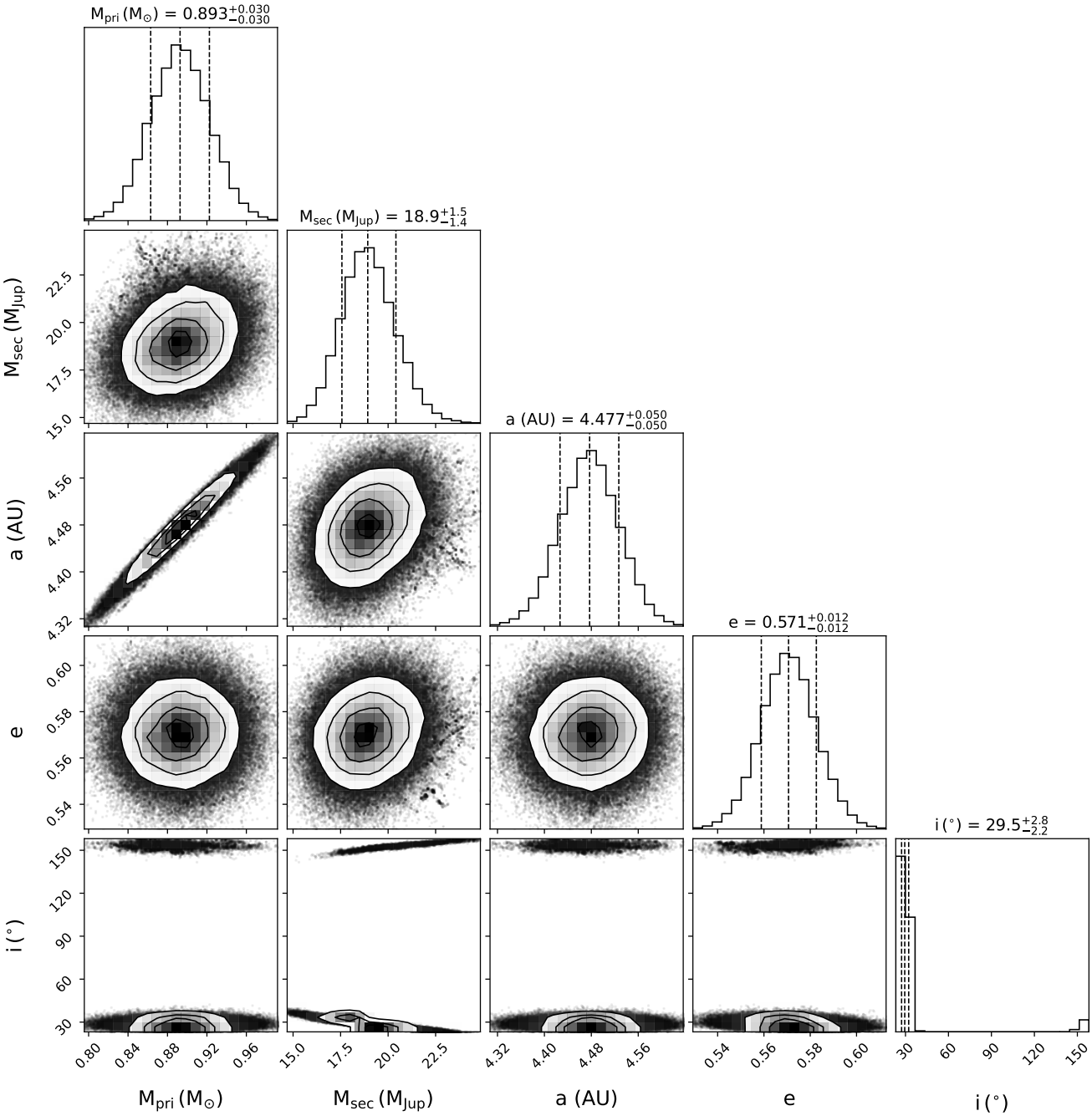

Figure A15. HD 106515 Ab. Same as Fig. A10.

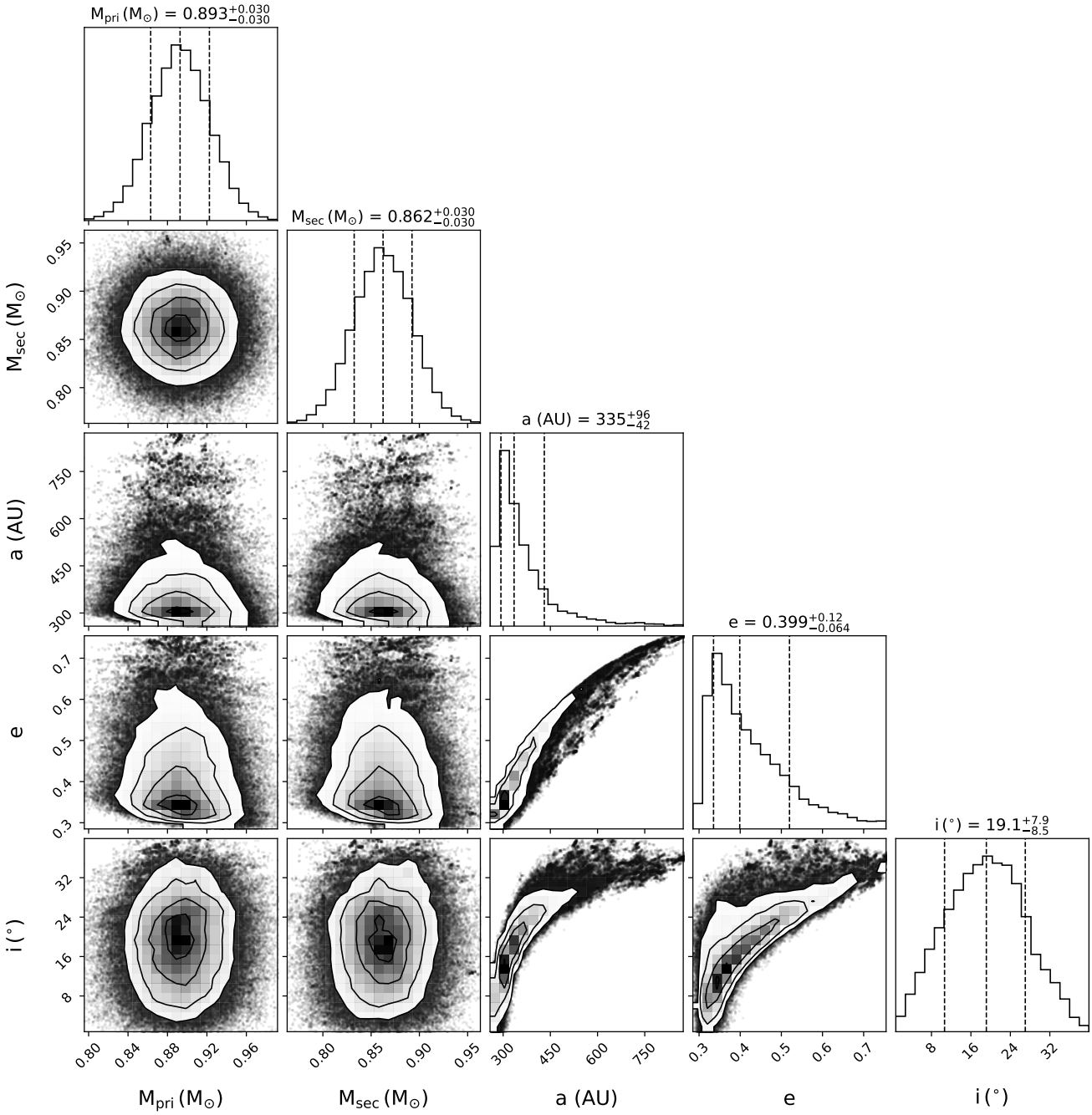

Figure A16. HD 106515 B, the stellar companion to HD 106515 A. Same as Fig. A10.

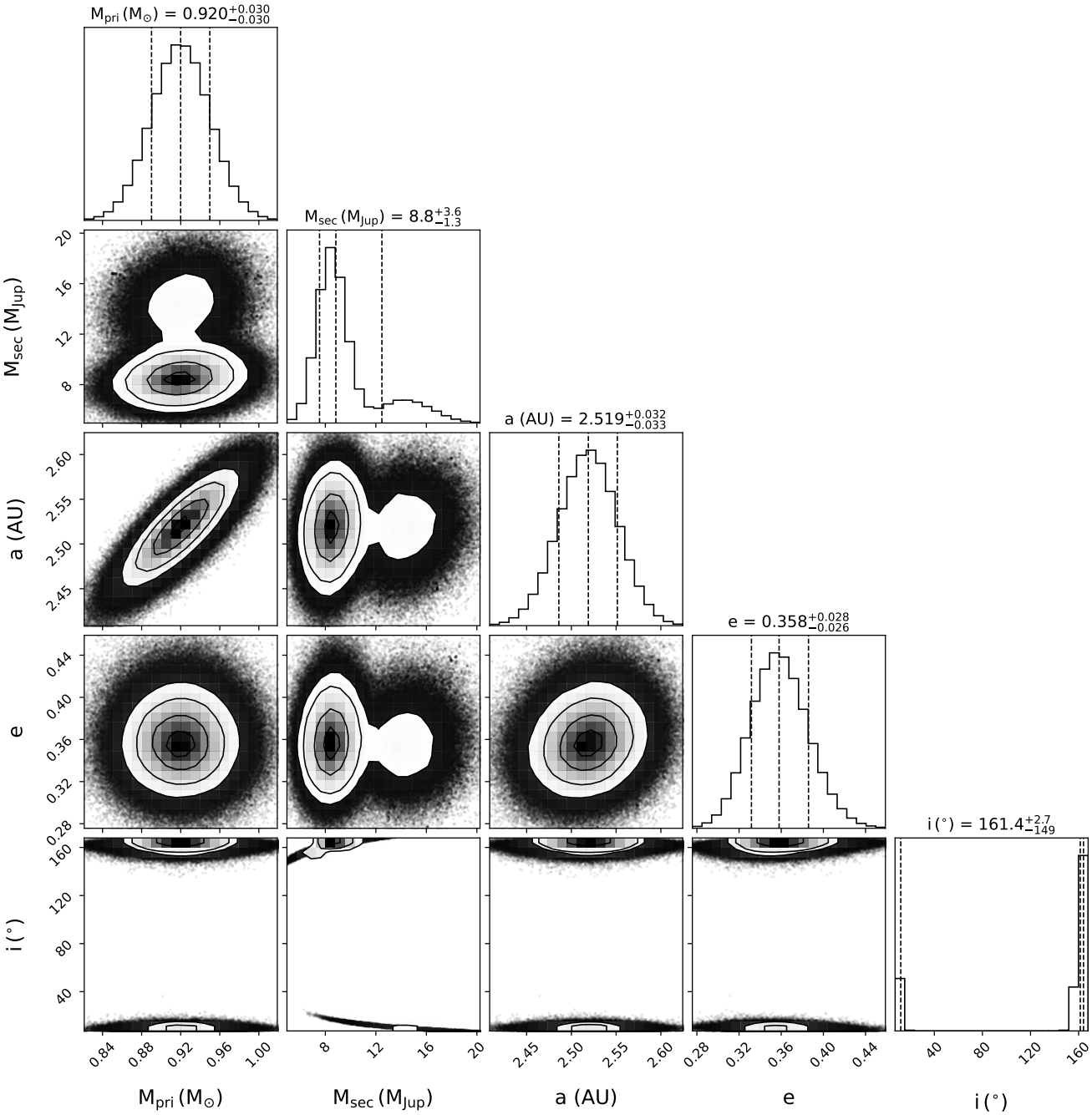

Figure A17. HD 171238 b. Same as Fig. A10.

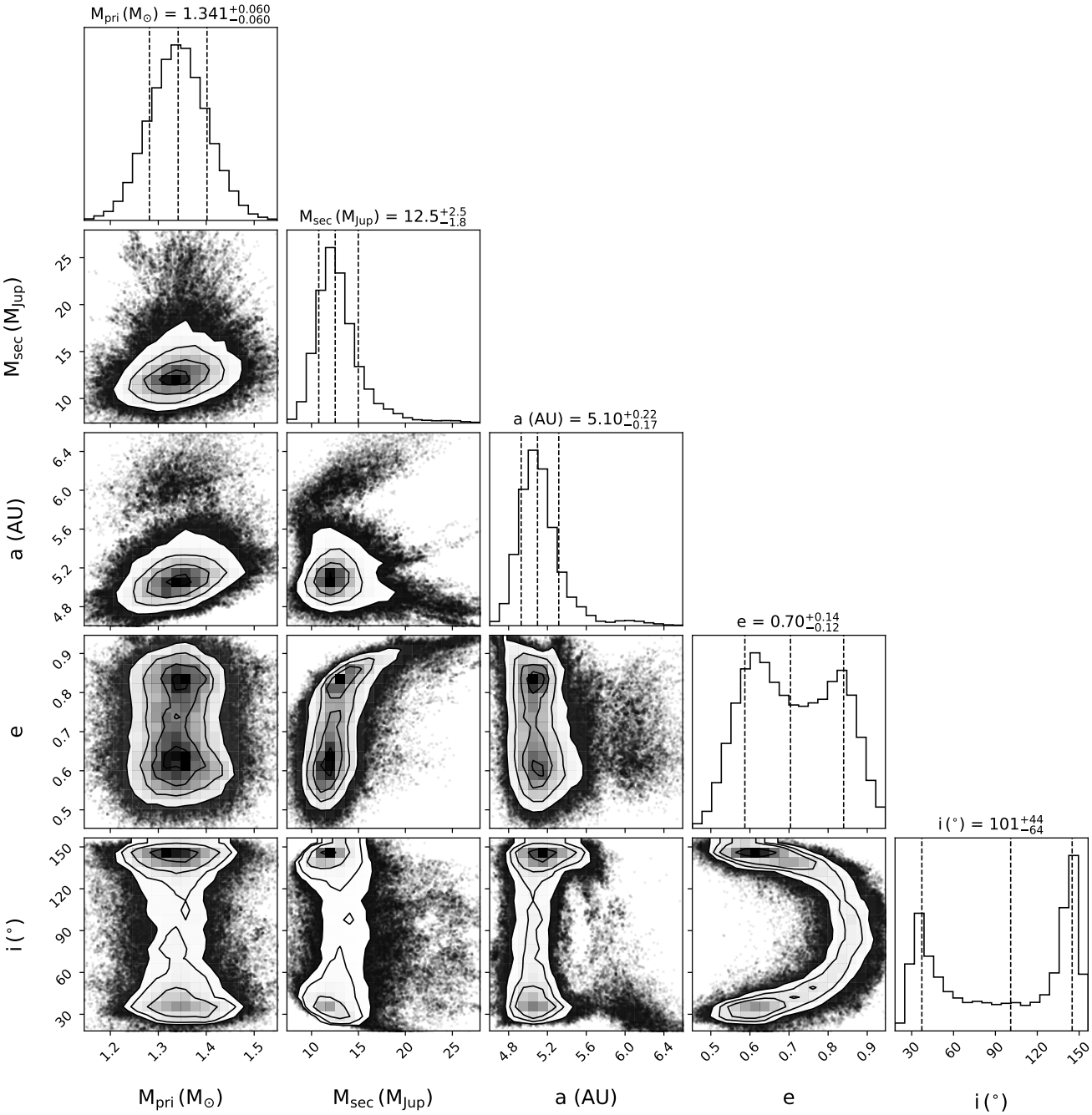

Figure A18. HD 196067 b. Same as Fig. A10.

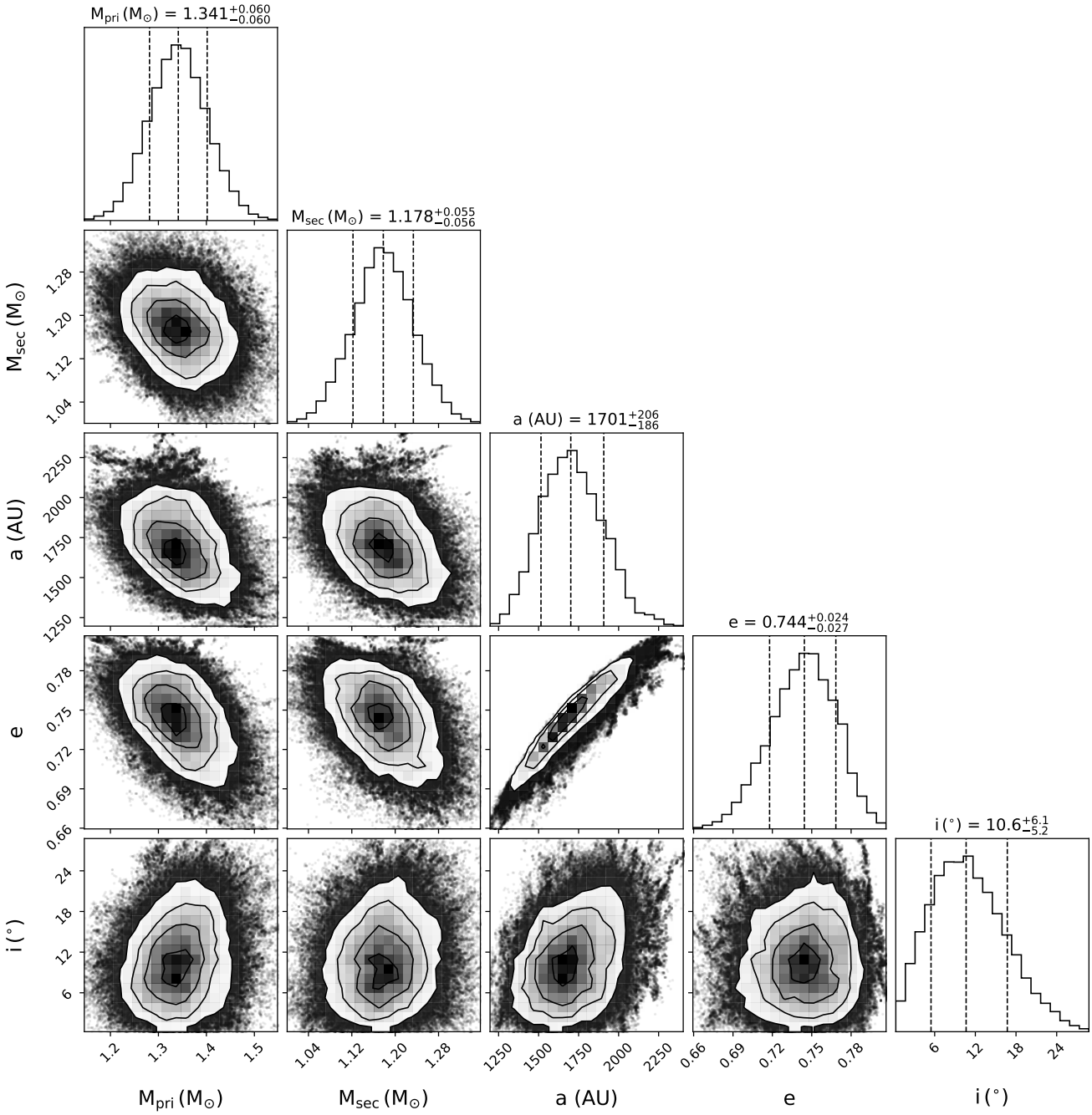

Figure A19. HD 196068. It is bound to HD 196067. Same as Fig. A10.

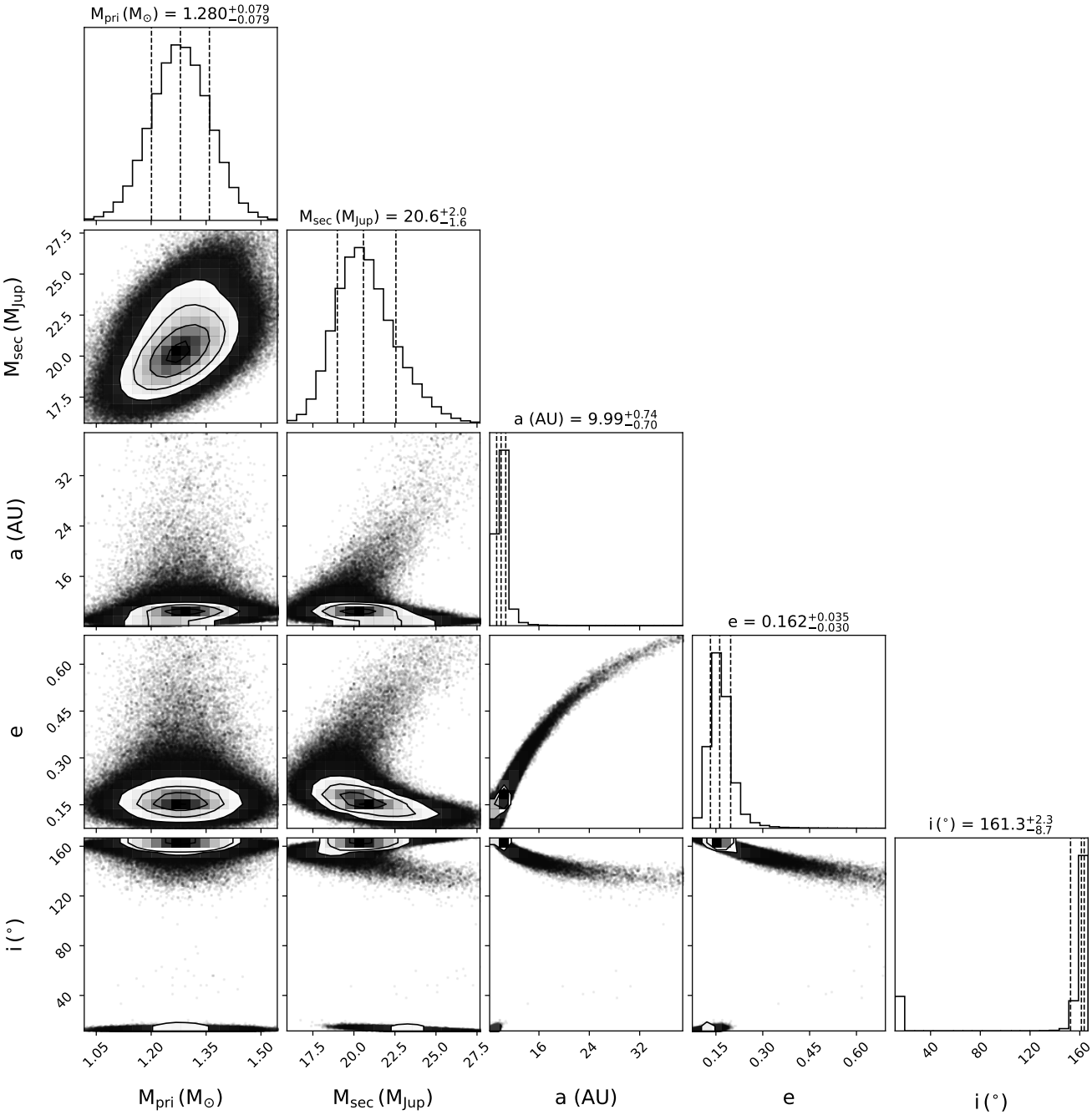

Figure A20. HD 221420 b. Same as Fig. A10.

REFERENCES

Adibekyan, V. Z., Figueira, P., Santos, N. C., et al. 2013, A&A, 560, A51

Aguilera-Gómez, C., Ramírez, I., & Chanamé, J. 2018, A&A, 614, A55

Akeson, R. L., Chen, X., Ciardi, D., et al. 2013, PASP, 125, 989

Allende Prieto, C., & Lambert, D. L. 1999, A&A, 352, 555

Anders, F., Khalatyan, A., Chiappini, C., et al. 2019, A&A, 628, A94

Anderson, E., & Francis, C. 2012, Astronomy Letters, 38, 331

Angus, R., Aigrain, S., Foreman-Mackey, D., & McQuillan, A. 2015, MNRAS, 450, 1787

Arriagada, P. 2011, ApJ, 734, 70

Barnes, S. A. 2003, ApJ, 586, 464

Barnes, S. A. 2007, ApJ, 669, 1167

Batalha, N. E., Lewis, T., Fortney, J. J., et al. 2019, ApJL, 885, L25

Bauer, F. F., Zechmeister, M., Kaminski, A., et al. 2020, A&A, 640, A50

Baumann, P., Ramírez, I., Meléndez, J., Asplund, M., & Lind, K. 2010, A&A, 519, A87

Benedict, G. F., McArthur, B. E., & Bean, J. L. 2008, IAU Symp., 248, 23

Benedict, G. F., McArthur, B. E., Fredrick, L. W., et al. 2002, AJ, 124, 1695

Benedict, G. F., McArthur, B. E., Gatewood, G., et al. 2006, The Astronomical Journal, 132, 2206

Beuzit, J.-L., Feldt, M., Dohlen, K., et al. 2008, in Society of Photo-Optical Instrumentation Engineers (SPIE) Conference Series, Vol. 7014, Ground-based and Airborne Instrumentation for Astronomy II, ed. I. S. McLean & M. M. Casali, 701418

Boffin, H. M. J., Rivinius, T., Mérand, A., et al. 2016, A&A, 593, A90

Bond, J. C., Tinney, C. G., Butler, R. P., et al. 2006, MNRAS, 370, 163

Bonfanti, A., Ortolani, S., & Nascimbeni, V. 2016, A&A, 585, A5

Bonfanti, A., Ortolani, S., Piotto, G., & Nascimbeni, V. 2015, A&A, 575, A18

Borgniet, S., Lagrange, A. M., Meunier, N., et al. 2019, A&A, 621, A87

Boss, A. P. 2008, The Astrophysical Journal, 677, 607

Bowler, B. P. 2016, PASP, 128, 102001

Bowler, B. P., Blunt, S. C., & Nielsen, E. L. 2020, AJ, 159, 63

Brandt, G. M., Brandt, T. D., Dupuy, T. J., Li, Y., & Michalik, D. 2021a, AJ, 161, 179

Brandt, G. M., Michalik, D., Brandt, T. D., et al. 2021b, arXiv e-prints, arXiv:2109.06761

Brandt, T. D. 2018, ApJS, 239, 31

Brandt, T. D. 2021, arXiv e-prints, arXiv:2103.07432

Brandt, T. D., Dupuy, T. J., & Bowler, B. P. 2019, The Astronomical Journal, 158, 140

Brandt, T. D., Dupuy, T. J., Bowler, B. P., et al. 2020, AJ, 160, 196

Brandt, T. D., Dupuy, T. J., Li, Y., et al. 2021c, arXiv e-prints, arXiv:2105.11671

Brandt, T. D., Kuzuhara, M., McElwain, M. W., et al. 2014, The Astrophysical Journal, 786, 1

Bressan, A., Marigo, P., Girardi, L., et al. 2012, MNRAS, 427, 127

Brewer, J. M., Fischer, D. A., Valenti, J. A., & Piskunov, N. 2016, ApJS, 225, 32

Brown, R. A. 2011, ApJ, 733, 68

Butler, R. P., Vogt, S. S., Laughlin, G., et al. 2017, AJ, 153, 208

Butler, R. P., Wright, J. T., Marcy, G. W., et al. 2006, ApJ, 646, 505

Cantat-Gaudin, T., & Brandt, T. D. 2021, arXiv e-prints, arXiv:2103.07432

Casagrande, L., Ramírez, I., Meléndez, J., Bessell, M., & Asplund, M. 2010, A&A, 512, A54

Casagrande, L., Schönrich, R., Asplund, M., et al. 2011, A&A, 530, A138

Chandler, C. O., McDonald, I., & Kane, S. R. 2016, AJ, 151, 59

Chauvin, G., Gratton, R., Bonnefoy, M., et al. 2018, A&A, 617, A76

Chauvin, G., Lagrange, A. M., Zuckerman, B., et al. 2005, A&A, 438, L29

Chilcote, J. K., Bailey, V. P., De Rosa, R., et al. 2018, in Society of Photo-Optical Instrumentation Engineers (SPIE) Conference Series, Vol. 10702, Ground-based and Airborne Instrumentation for Astronomy VII, ed. C. J. Evans, L. Simard, & H. Takami, 1070244

Cumming, A. 2004, Monthly Notices of the Royal Astronomical Society, 354, 1165

Cutri, R. M., Skrutskie, M. F., van Dyk, S., et al. 2003, VizieR Online Data Catalog, II/246

Datson, J., Flynn, C., & Portinari, L. 2012, MNRAS, 426, 484

Datson, J., Flynn, C., & Portinari, L. 2015, A&A, 574, A124

David, T. J., & Hillenbrand, L. A. 2015, ApJ, 804, 146

Delgado Mena, E., Bertrán de Lis, S., Adibekyan, V. Z., et al. 2015, A&A, 576, A69

Desidera, S., Gratton, R., Carolo, E., et al. 2012, A&A, 546, A108
Diego, F., Charalambous, A., Fish, A. C., & Walker, D. D. 1990, in Society of Photo-Optical Instrumentation Engineers (SPIE) Conference Series, Vol. 1235, Instrumentation in Astronomy VII, ed. D. L. Crawford, 562
Dommanget, J., & Nys, O. 2002, VizieR Online Data Catalog, I/274
Eisner, J. A., & Kulkarni, S. R. 2001, ApJ, 550, 871
ESA, ed. 1997, ESA Special Publication, Vol. 1200, The HIPPARCOS and TYCHO catalogues. Astrometric and photometric star catalogues derived from the ESA HIPPARCOS Space Astrometry Mission
Feng, F., Anglada-Escudé, G., Tuomi, M., et al. 2019, MNRAS, 490, 5002
Fischer, D., Driscoll, P., Isaacson, H., et al. 2009, ApJ, 703, 1545
Fischer, D. A., Anglada-Escude, G., Arriagada, P., et al. 2016, PASP, 128, 066001
Fischer, D. A., Marcy, G. W., Butler, R. P., et al. 2002, PASP, 114, 529
Fischer, D. A., Marcy, G. W., & Spronck, J. F. P. 2013, The Astrophysical Journal Supplement Series, 210, 5
Fischer, D. A., & Valenti, J. 2005, ApJ, 622, 1102
Ford, E. B. 2014, Proceedings of the National Academy of Sciences, 111, 12616
Foreman-Mackey, D., Hogg, D. W., Lang, D., & Goodman, J. 2013, PASP, 125, 306
Fuhrmann, K. 2008, MNRAS, 384, 173
Gaia Collaboration. 2020, VizieR Online Data Catalog, I/350
Gaia Collaboration, Brown, A. G. A., Vallenari, A., et al. 2018, A&A, 616, A1
Gaia Collaboration, Brown, A. G. A., Vallenari, A., et al. 2020, Gaia Early Data Release 3: Summary of the contents and survey properties
Gaidos, E., Mann, A. W., Kraus, A. L., & Ireland, M. 2016, MNRAS, 457, 2877
Gáspár, A., Rieke, G. H., & Ballering, N. 2016, ApJ, 826, 171
Gaudi, B. S. 2021, arXiv e-prints, arXiv:2102.01715
Ginski, C., Mugrauer, M., Seeliger, M., & Eisenbeiss, T. 2012, Monthly Notices of the Royal Astronomical Society, 421, 2498
Goda, S., & Matsuo, T. 2019, ApJ, 876, 23
Golub, L. 1996, Ap&SS, 237, 33
Gomes da Silva, J., Santos, N. C., Adibekyan, V., et al. 2021, A&A, 646, A77
Gondoin, P. 2020, A&A, 641, A110
Gontcharov, G. A. 2012, Astronomy Letters, 38, 771
Gonzalez, G., Carlson, M. K., & Tobin, R. W. 2010, MNRAS, 403, 1368
González Hernández, J. I., Israelian, G., Santos, N. C., et al. 2010, ApJ, 720, 1592
Gould, A., & Chaname, J. 2004, The Astrophysical Journal Supplement Series, 150, 455
Grandjean, A., Lagrange, A. M., Beust, H., et al. 2019, A&A, 627, L9
Gravity Collaboration, Abuter, R., Accardo, M., et al. 2017, A&A, 602, A94
Gray, R. O., Corbally, C. J., Garrison, R. F., McFadden, M. T., & Robinson, P. E. 2003, AJ, 126, 2048
Güdel, M. 2004, A&A Rv, 12, 71
Hall, J. C. 2008, Living Reviews in Solar Physics, 5, 2
Han, I., Black, D. C., & Gatewood, G. 2001, The Astrophysical Journal, 548, L57
Hatzes, A. P. 2016, The Radial Velocity Method for the Detection of Exoplanets, ed. V. Bozza, L. Mancini, & A. Sozzetti, Vol. 428 3
He, M. Y., Ford, E. B., & Ragozzine, D. 2020, The Astronomical Journal, 161, 16
Heiter, U., & Luck, R. E. 2003, AJ, 126, 2015
Herrero, E., Ribas, I., Jordi, C., Guinan, E. F., & Engle, S. G. 2012, A&A, 537, A147
Høg, E., Fabricius, C., Makarov, V. V., et al. 2000, A&A, 355, L27
Holmberg, J., Nordström, B., & Andersen, J. 2009, A&A, 501, 941
Howard, A. W., Marcy, G. W., Bryson, S. T., et al. 2012, ApJS, 201, 15
Howard, A. W., Marcy, G. W., Johnson, J. A., et al. 2010, Science, 330, 653
Hsu, D. C., Ford, E. B., Ragozzine, D., & Ashby, K. 2019, The Astronomical Journal, 158, 109
Huang, C., Zhao, G., Zhang, H. W., & Chen, Y. Q. 2005, MNRAS, 363, 71
Ireland, M. J., Kraus, A., Martinache, F., Law, N., & Hillenbrand, L. A. 2010, The Astrophysical Journal, 726, 113
Isaacson, H., & Fischer, D. 2010, ApJ, 725, 875
Jardine, M., Wood, K., Collier Cameron, A., Donati, J. ., & Mackay, D. H. 2002, Monthly Notices of the Royal Astronomical Society, 336, 1364
Jenkins, J. S., Jones, H. R. A., Pavlenko, Y., et al. 2008, A&A, 485, 571
Jenkins, J. S., Murgas, F., Rojo, P., et al. 2011, A&A, 531, A8
Jin, S. 2021, arXiv e-prints, arXiv:2102.05808
Jofré, E., Petrucci, R., Saffe, C., et al. 2015, A&A, 574, A50

Kane, S. R., Dalba, P. A., Li, Z., et al. 2019, AJ, 157, 252
Kang, W., Lee, S.-G., & Kim, K.-M. 2011, ApJ, 736, 87
Kasdin, N. J., Bailey, V. P., Mennesson, B., et al. 2020, in Society of Photo-Optical Instrumentation Engineers (SPIE) Conference Series, Vol. 11443, Society of Photo-Optical Instrumentation Engineers (SPIE) Conference Series, 114431U
Kervella, P., Arenou, F., Mignard, F., & Thévenin, F. 2019, A&A, 623, A72
Kervella, P., Arenou, F., & Schneider, J. 2020, A&A, 635, L14
Kiefer, F., Hébrard, G., Lecavelier des Etangs, A., et al. 2021, A&A, 645, A7
Kim, B., An, D., Stauffer, J. R., et al. 2016, ApJS, 222, 19
Knutson, H. A., Fulton, B. J., Montet, B. T., et al. 2014, The Astrophysical Journal, 785, 126
Kotoneva, E., Shi, J. R., Zhao, G., & Liu, Y. J. 2006, A&A, 454, 833
Kozai, Y. 1962, AJ, 67, 591
Kraft, R. P. 1967, ApJ, 150, 551
Lafrenière, D., Jayawardhana, R., & van Kerkwijk, M. H. 2008, ApJL, 689, L153
Lagrange, A.-M. 2014, Philosophical transactions. Series A, Mathematical, physical, and engineering sciences, 372, 20130090
Lanza, A. F., Malavolta, L., Benatti, S., et al. 2018, A&A, 616, A155
Laws, C., Gonzalez, G., Walker, K. M., et al. 2003, AJ, 125, 2664
Lidov, M. L. 1962, Planet. Space Sci., 9, 719
Lindegren, L., & Dravins, D. 2003, A&A, 401, 1185
Lindegren, L., Klioner, S. A., Hernández, J., et al. 2020, arXiv e-prints, arXiv:2012.03380
Lineweaver, C. H., & Grether, D. 2003, The Astrophysical Journal, 598, 1350
Liu, K., Bi, S.-L., Li, T.-D., et al. 2014, Research in Astronomy and Astrophysics, 14, 1447
Lorenzo-Oliveira, D., Porto de Mello, G. F., Dutra-Ferreira, L., & Ribas, I. 2016, A&A, 595, A11
Luck, R. E. 2017, AJ, 153, 21
Luck, R. E., & Heiter, U. 2006, AJ, 131, 3069
Maldonado, J., Eiroa, C., Villaver, E., Montesinos, B., & Mora, A. 2012, A&A, 541, A40
Maldonado, J., & Villaver, E. 2016, A&A, 588, A98
Maldonado, J., Villaver, E., Eiroa, C., & Micela, G. 2019, A&A, 624, A94
Mamajek, E. E., & Hillenbrand, L. A. 2008, ApJ, 687, 1264
Marchi, S. 2007, ApJ, 666, 475
Marchwinski, R. C., Mahadevan, S., Robertson, P., Ramsey, L., & Harder, J. 2014, The Astrophysical Journal, 798, 63
Marmier, M., Ségransan, D., Udry, S., et al. 2013, A&A, 551, A90
Marois, C., Macintosh, B., Barman, T., et al. 2008, Science, 322, 1348
Marsakov, V. A., & Shevelev, Y. G. 1995, Bulletin d'Information du Centre de Donnees Stellaires, 47, 13
Mayor, M., & Queloz, D. 1995, Nature, 378, 355
McArthur, B. E., Benedict, G. F., Barnes, R., et al. 2010, The Astrophysical Journal, 715, 1203
Ment, K., Fischer, D. A., Bakos, G., Howard, A. W., & Isaacson, H. 2018, AJ, 156, 213
Metchev, S. A., & Hillenbrand, L. A. 2009, The Astrophysical Journal Supplement Series, 181, 62
Meunier, N., & Lagrange, A. M. 2019, A&A, 628, A125
Mewe, R. 1996, SoPh, 169, 335
Mints, A., & Hekker, S. 2017, A&A, 604, A108
Mishenina, T. V., Soubiran, C., Bienaymé, O., et al. 2008, A&A, 489, 923
Montes, D., López-Santiago, J., Gálvez, M., et al. 2001, Monthly Notices of the Royal Astronomical Society, 328, 45
Mortier, A., Santos, N. C., Sousa, S., et al. 2013, A&A, 551, A112
Mugrauer, M. 2019, MNRAS, 490, 5088
Nielsen, E. L., De Rosa, R. J., Wang, J. J., et al. 2020, AJ, 159, 71
Noyes, R. W., Hartmann, L. W., Baliunas, S. L., Duncan, D. K., & Vaughan, A. H. 1984, ApJ, 279, 763
Oelkers, R. J., Rodriguez, J. E., Stassun, K. G., et al. 2018, AJ, 155, 39
Pace, G. 2013, A&A, 551, L8
Parker, E. N. 1955, ApJ, 122, 293
Parker, E. N. 1979, Cosmical magnetic fields. Their origin and their activity, Oxford: Clarendon Press, 1979.
Perrier, C., Sivan, J. P., Naef, D., et al. 2003, A&A, 410, 1039
Phillips, M. W., Tremblin, P., Baraffe, I., et al. 2020, A&A, 637, A38
Plavchan, P., Latham, D., Gaudi, S., et al. 2015, Radial velocity prospects current and future: A white paper report prepared by the study analysis group 8 for the exoplanet program analysis group (exopag)
Porto de Mello, G. F., da Silva, R., da Silva, L., & de Nader, R. V. 2014, A&A, 563, A52
Queiroz, A. B. A., Anders, F., Chiappini, C., et al. 2020, A&A, 638, A76
Rameau, J., Chauvin, G., Lagrange, A.-M., et al. 2013, The Astrophysical Journal Letters
Ramírez, I., Meléndez, J., Bean, J., et al. 2014, A&A, 572, A48

Reffert, S., & Quirrenbach, A. 2011, A&A, 527, A140
Reinhold, T., & Hekker, S. 2020, A&A, 635, A43
Rey, J., Hébrard, G., Bouchy, F., et al. 2017, A&A, 601, A9
Rica, F. M., Barrena, R., Henríquez, J. A., Pérez, F. M., & Vargas, P. 2017, Publications of the Astronomical Society of Australia, 34, e004
Rice, K. 2014, Challenges, 5, 296
Rich, E. A., Wisniewski, J. P., McElwain, M. W., et al. 2017, MNRAS, 472, 1736
Rickman, E. L., Ségransan, D., Marmier, M., et al. 2019, A&A, 625, A71
Sadakane, K., Ohkubo, M., Takeda, Y., et al. 2002, PASJ, 54, 911
Saffe, C., Jofré, E., Miquelarena, P., et al. 2019, A&A, 625, A39
Sahlmann, J., Ségransan, D., Queloz, D., et al. 2011, A&A, 525, A95
Santos, N. C., Adibekyan, V., Figueira, P., et al. 2017, A&A, 603, A30
Santos, N. C., Israelian, G., & Mayor, M. 2004, A&A, 415, 1153
Santos, N. C., Israelian, G., Mayor, M., et al. 2005, A&A, 437, 1127
Santos, N. C., Israelian, G., Mayor, M., Rebolo, R., & Udry, S. 2003, A&A, 398, 363
Santos, N. C., Sousa, S. G., Mortier, A., et al. 2013, A&A, 556, A150
Schatzman, E. 1962, Annales d'Astrophysique, 25, 18
Schatzman, E. 1990, International Astronomical Union Colloquium, 121, 5–17
Schlaufman, K. C. 2018, ApJ, 853, 37
Schröder, C., Reiners, A., & Schmitt, J. H. M. M. 2009, A&A, 493, 1099
Ségransan, D., Udry, S., Mayor, M., et al. 2010, A&A, 511, A45
Skiff, B. A. 2014, VizieR Online Data Catalog, B/mk
Skrutskie, M. F., Cutri, R. M., Stiening, R., et al. 2006, AJ, 131, 1163
Skumanich, A. 1972, ApJ, 171, 565
Snellen, I. A. G., & Brown, A. G. A. 2018, Nature Astronomy, 2, 883
Soderblom, D. R. 2010, ARA&A, 48, 581
Soderblom, D. R., Duncan, D. K., & Johnson, D. R. H. 1991, ApJ, 375, 722
Soto, M. G., & Jenkins, J. S. 2018, A&A, 615, A76
Soubiran, C., Le Campion, J.-F., Brouillet, N., & Chemin, L. 2016, A&A, 591, A118
Sousa, S. G., Adibekyan, V., Delgado-Mena, E., et al. 2018, A&A, 620, A58
Sousa, S. G., Santos, N. C., Israelian, G., Mayor, M., & Monteiro, M. J. P. F. G. 2006, A&A, 458, 873
Sousa, S. G., Santos, N. C., Mayor, M., et al. 2008, A&A, 487, 373
Sozzetti, A., & Desidera, S. 2010, A&A, 509, A103
Sozzetti, A., Udry, S., Zucker, S., et al. 2006, A&A, 449, 417
Spiegel, D. S., Burrows, A., & Milsom, J. A. 2011, ApJ, 727, 57
Spina, L., Meléndez, J., & Ramírez, I. 2016, A&A, 585, A152
Stassun, K. G., Collins, K. A., & Gaudi, B. S. 2017, AJ, 153, 136
Stassun, K. G., Oelkers, R. J., Paegert, M., et al. 2019, AJ, 158, 138
Strassmeier, K., Washuettl, A., Granzer, T., Scheck, M., & Weber, M. 2000, A&AS, 142, 275
Takeda, G., Ford, E. B., Sills, A., et al. 2007, ApJS, 168, 297
Testa, P., Saar, S., & Drake, J. 2015, Philosophical transactions. Series A, Mathematical, physical, and engineering sciences, 373
Trifonov, T., Tal-Or, L., Zechmeister, M., et al. 2020, A&A, 636, A74
Tsantaki, M., Sousa, S. G., Adibekyan, V. Z., et al. 2013, A&A, 555, A150
Udry, S., Fischer, D., & Queloz, D. 2007, Protostars and Planets V
Valenti, J. A., & Fischer, D. A. 2005, ApJS, 159, 141
van Leeuwen, F. 2007, A&A, 474, 653
van Saders, J. L., Ceillier, T., Metcalfe, T. S., et al. 2016, Nature, 529, 181
Venner, A., Vanderburg, A., & Pearce, L. A. 2021, arXiv e-prints, arXiv:2104.13941
Voges, W., Aschenbach, B., Boller, T., et al. 1999, A&A, 349, 389
Voges, W., Aschenbach, B., Boller, T., et al. 2000, IAUC, 7432, 3
Vousden, W. D., Farr, W. M., & Mandel, I. 2016, MNRAS, 455, 1919
Walker, G. A. 2012, New Astronomy Reviews, 56, 9, Exoplanets: Birth of a New Field of Study
Wei, J. 2018, arXiv e-prints, arXiv:1805.02771
White, R. J., Gabor, J. M., & Hillenbrand, L. A. 2007, AJ, 133, 2524
Wilson, O. C. 1968, ApJ, 153, 221
Winter, A. J., Kruijssen, J. M. D., Longmore, S. N., & Chevance, M. 2020, Nature, 586, 528
Wittenmyer, R. A., Butler, R. P., Tinney, C. G., et al. 2016, ApJ, 819, 28

Wittenmyer, R. A., Endl, M., Cochran, W. D., Levison, H. F., & Henry, G. W. 2009, ApJS, 182, 97

Wright, C. O., Egan, M. P., Kraemer, K. E., & Price, S. D. 2003, AJ, 125, 359

Wright, J. T. 2018, Handbook of Exoplanets, 619–631

Yee, S. W., Petigura, E. A., & von Braun, K. 2017, ApJ, 836, 77

Zhuleku, J., Warnecke, J., & Peter, H. 2020, A&A, 640, A119